Discerning singlet and triplet scalars at the electroweak phase transition and gravitational wave

Priyotosh Bandyopadhyay[1,*] and Shilpa Jangid[1,2,†,‡]

[1]*Indian Institute of Technology Hyderabad, Kandi, Sangareddy-502284, Telangana, India*
[2]*Asia Pacific Center for Theoretical Physics, Pohang, 37673, Korea*

(Received 29 January 2022; accepted 6 March 2023; published 21 March 2023)

In this article, we examine the prospect of a first-order phase transition with a $Y = 0$ real $SU(2)$ triplet extension of the Standard Model, which remains odd under Z_2, considering the observed Higgs boson mass, perturbative unitarity, dark matter constraints, etc. Especially, we investigate the role of Higgs-triplet quartic coupling considering one- and two-loop beta functions and compare the results with the complex singlet extension case. It is observed that, at one-loop level, no solution can be found for both, demanding Planck-scale perturbativity. However, for a much lower scale of 10^4 GeV, the singlet case predicts a first-order phase transition consistent with the observed Higgs boson mass. On the contrary, for the two-loop beta functions with one-loop potential, both the scenarios foresee a strongly first-order phase transition consistent with the observed Higgs mass with upper bounds of 310 and 909 GeV on the triplet and singlet masses, respectively. This mass bound shifts to 259 GeV in the case of a triplet with the inclusion of two-loop contributions to the effective potential and the thermal masses with two-loop beta functions, consistent with Planck-scale perturbativity and the observed Higgs boson mass value. This puts the triplet in apparent contradiction with the observed dark matter relic bound and, thus, requires an additional field for that. The preferred regions of the parameter space in both cases are identified by benchmark points that predict gravitational waves with detectable frequencies in present and future experiments.

DOI: 10.1103/PhysRevD.107.055032

I. INTRODUCTION

The discovery of the Higgs boson around 125.5 GeV was the last stepping stone in the Standard Model (SM) [1,2] and a proof of spontaneous symmetry breaking in generating the masses of some of the SM particles. However, the nature of symmetry breaking is far from understood; i.e., the role of another scalar, the order of phase transition, etc., are still to be comprehended. It is intriguing to notice that, with one Higgs doublet and the Higgs boson mass around 125.5 GeV, one finds only a smooth crossover [3–7] but not the first-order phase transition. The requirement of the first-order phase transition is vastly related to the observed baryon number and lepton number in today's Universe [8–10]. This pushes for an additional scalar(s) along with the SM Higgs doublet. The requirement of an additional scalar can also be justified, as, in the SM, there is no cold dark matter (DM) candidate, and it can also provide the much-needed stability of the electroweak vacuum of the SM and its various seesaw extensions [11–14]. It is also interesting to see if these additional scalars are consistent with various constraints coming from the collider experiments, dark matter relic abundance along with the requirement of the strongly first-order phase transition. The inspections regarding the first-order phase transition exist in various possible extensions of the SM, viz. in supersymmetric scenarios [15–28], inert doublet model [29–33], scalar singlet [34–50], two-Higgs-doublet model [51–54], triplet [55–59], and multiple fields [60–64]. Some of these extensions need a revisit considering various recent experimental constraints along with theoretical perturbative unitarity.

The first-order phase transition originates from the bubble nucleation of the true vacuum at the nucleation temperature T_n. These bubbles expand due to the pressure difference between the true and the false vacua, and the broken phase extends to the unbroken phase outside [65]. During such bubble expansion in the first-order phase transition, bubbles collide and create gravitational waves (GWs) [65–73]. Different scenarios foretelling the first-order phase transition generate different GW frequencies that can be detected by the various present and future experiments.

*bpriyo@phy.iith.ac.in
†ph19resch02006@iith.ac.in
‡shilpa.jangid@apctp.org

It would be interesting to see if such different extensions can be distinguished either theoretically or experimentally. We are particularly interested in the study of SM extension with a $Y = 0$ $SU(2)$ triplet, which stabilizes the electroweak vacuum till the Planck scale [12], and compare the results with a singlet extension. Such a triplet, odd under Z_2, provides the much-needed dark matter in terms of its neutral component, which should be $\lesssim 1.2$ TeV to satisfy the DM relic abundance [12]. The scenario is especially interesting, as it provides a charged Higgs boson with displaced decays, which can be detected in the LHC and the Massive Timing Hodoscope for Ultrastable Neutral Particles (MATHUSLA) [12,74,75]. In the context of supersymmetry, the $Y = 0$ triplet is also motivated for the reappearance of TeV-scale supersymmetry consistent with a 125.5 GeV Higgs boson [76–78], predicting correct $B \to X_s\gamma$ [76,79], triplet charged Higgs boson [80–82], and displaced decays of triplinos [83].

In this article, we explore the possibility of such a triplet, providing the much-needed strongly first-order phase transition and the corresponding bound on the triplet mass parameter. The compatibility with perturbative unitary at one- and two-loop level is also studied along with the bounds from the Higgs data and DM relic. The scenario is also compared with the complex singlet extension of the SM, which is also odd under Z_2 [84]. Finally, by measuring the bubble nucleation temperature along with other parameters, we estimate the signal frequencies of the GWs created by the bubble collisions. Along with this, the sound wave of the plasma and the turbulence contribute substantially and are also considered here. Such frequencies can be detected by various future space interferometer experiments like Big Bang Observer (BBO) [85], Laser Interferometer Space Antenna (LISA) [86], and Earth-based detector Laser Interferometer Gravitational Wave Observatory (LIGO) [87–89], and such regions are identified.

The article is organized as follows. In Secs. II and III, we describe the inert singlet and inert triplet model along with the calculation of thermal-corrected potential and masses with broadly defining the regions responsible for first-order phase transition. The critical temperature and the effect of the quartic couplings are discussed in Sec. IV. The bounds from perturbative unitarity at one and two loops, DM relics are discussed in Sec. V. The frequencies for the gravitational waves and their detectability in various experiments for different benchmark points are discussed in Sec. VII. Finally, we conclude in Sec. VIII.

II. CALCULATION OF FINITE TEMPERATURE POTENTIAL FOR INERT SINGLET SCENARIO

The minimal SM is extended with a complex singlet which is considered to be odd under the Z_2 symmetry. The SM Higgs doublet H is even under the Z_2 symmetry and transforms as $H \to H$, whereas the singlet S goes to $-S$. Being odd under Z_2, the neutral component of the singlet becomes the dark matter candidate. The detailed calculation of the tree-level mass spectrum and the vacuum stability analysis at zero temperature are given in Ref. [12]. The corresponding tree-level scalar potential is given by[1]

$$\begin{aligned} V &= -\mu^2 H^\dagger H + m_S^2 S^* S + \lambda_1 |H^\dagger H|^2 + \lambda_s |S^* S|^2 \\ &\quad + \lambda_{hs}(H^\dagger H)(S^* S), \\ H &= \begin{pmatrix} G^+ \\ \frac{1}{\sqrt{2}}(\phi + h) + iG^0 \end{pmatrix}, \end{aligned} \tag{2.1}$$

where neutral component ϕ, of the SM Higgs doublet H, acts as the background field. However, in the case of the SM, the field-dependent masses for Higgs field h, Goldstone bosons G^0, the gauge bosons ($W^\pm$ and Z boson), and the dominant top quark contribute to the effective potential. The expressions for the field-dependent mass contributing to the effective potential from the SM are given as follows:

$$\begin{aligned} &M_h^2(\phi) = 3\lambda_1\phi^2 - \mu^2, \qquad M_{G^0}^2 = \lambda_1\phi^2 - \mu^2, \\ &M_W^2(\phi) = \frac{g_2}{4}\phi^2, \qquad M_Z^2(\phi) = \frac{(g_2 + g_1)}{4}\phi^2, \\ &M_t^2(\phi) = \frac{y_t^2}{2}\phi^2, \end{aligned} \tag{2.2}$$

where M_t is defined as the top-quark mass. As the singlet does not acquire a vacuum expectation value (VEV), the field-dependent masses for the singlet will be given in terms of SM background field ϕ only. The field-dependent mass of singlet contributing to the effective potential is calculated as

$$M_S^2(\phi) = m_S^2 + \frac{\lambda_{hs}}{2}\phi^2. \tag{2.3}$$

The one-loop daisy-improved finite temperature effective potential can be written as [16,84]

$$\begin{aligned} V_{\text{eff}}(\phi, T) &= V_0(\phi) + V_1(\phi, 0) + \Delta V_1(\phi, T) \\ &\quad + \Delta V_{\text{daisy/ring}}(\phi, T), \end{aligned} \tag{2.4}$$

where $V_0(\phi)$ corresponds to the tree-level potential $V_{\text{tree}}(\phi)$:

$$V_0(\phi) = V_{\text{tree}}(\phi) = \frac{-\mu^2}{2}\phi^2 + \frac{\lambda_1}{4}\phi^4. \tag{2.5}$$

[1]This is our notation to use Higgs singlet interaction coupling as λ_{hs}, and this quartic coupling is defined as $\lambda_{hs} = 2\zeta^2$ in Ref. [84].

Here, $V_1(\phi,0)$ is evaluated at one loop at zero temperature via the Coleman-Weinberg prescription [90]. $\Delta V_1(\phi,T)$ presents the one-loop temperature-corrected potential. The potential without daisy resummation can be written as

$$V_{\rm tot} = V_0(\phi) + V_1(\phi,0) + \Delta V_1(\phi,T). \tag{2.6}$$

The total one-loop result $[V_{\rm eff}(\phi,T)]$ includes the resummation over a subclass of thermal loops which are defined as ring diagrams or daisy diagrams, and the plasma effects are explained by these ring-improved one-loop effective potentials [91–96]. These ring diagrams mainly amount to adding thermal corrections to bosons using ΔV_B. But this method of adding thermal corrections or resummation is not uniquely defined, and there are two different methods for adding such thermal corrections; one is the Parwani method, and the second one is the Arnold-Espinosa method [97]. In Arnold-Espinosa method, $M^2(\phi) \to M^2(\phi,T) = \mathcal{M}^2(\phi)$ is done only for the cubic term as in Eq. (2.6) and not for every term of the effective potential to obtain the ring-improved effective potential

$$V_{\rm daisy/ring} = V_{\rm tot}[M^2(\phi)] + \frac{T}{12\pi}\sum_{\rm bosons}(M^3(\phi) - M^3(\phi,T)) \quad \text{Arnold-Espinosa method.} \tag{2.7}$$

In the case of the Parwani method, $M^2(\phi) \to M^2(\phi,T) = \mathcal{M}^2(\phi)$ is done for each term in the effective potential as shown below:

$$V_{\rm ring} = V_{\rm tot}[M^2(\phi,T)] \quad \text{Parwani method.} \tag{2.8}$$

Therefore, there is a difference of two-loop order terms in these two prescriptions and can give us an idea about the uncertainties in our calculations if we neglect the higher-order terms in the perturbation theory. However, for this analysis we consider the Arnold-Espinosa prescription via considering thermal replacement of mass for the cubic mass terms only. Since fermions do not contribute in the cubic term, such replacements are ignored here.

The effective potential in the high-temperature limit includes ϕ depending mass contributions from bosons and fermions of the SM and singlet can be written as

$$V_{\rm eff}(\phi,T) = V_{\rm tree}(\phi,0) + \Delta V_B(\phi,T) + \Delta V_F(\phi,T), \tag{2.9}$$

where $V_{\rm tree}(\phi,0)$ is the tree-level potential and $\Delta V_B(\phi,T)$ is the one-loop contribution including thermal corrections from bosons. These one-loop contributions from bosons are defined as

$$\Delta V_B = \sum_{i=h,G,W_L,Z_L,\gamma_L,W_T,Z_T,\gamma_T,S} n_i \Delta V_i, \tag{2.10}$$

where $G \in \{G^0, G^\pm\}$ and W_L, Z_L, γ_L, W_T, Z_T, and γ_T are the longitudinal and transverse components of gauge bosons $W^\pm$ and Z and photon γ with ΔV_i as detailed below:

$$\Delta V_i = \frac{m_i^2(\phi)T^2}{24} - \frac{\mathcal{M}_i^3(\phi)T}{12\pi} - \frac{m_i^4(\phi)}{64\pi^2} \times \left[\log\frac{m_i^2(v)}{c_B T^2} - 2\frac{m_i^2(v)}{m_i^2(\phi)} + \delta_{iG}\log\frac{m_h^2(v)}{m_i^2(v)}\right]. \tag{2.11}$$

As mentioned earlier, for fermions only the dominant contribution from the top quark is considered in $\Delta V_F(\phi,T)$, and it does not have any cubic term, so no thermal corrections to masses are considered here as shown below:

$$\Delta V_F = n_t\left[\frac{m_t^2(\phi)T^2}{48} + \frac{m_t^4(\phi)}{64\pi^2}\left[\log\frac{m_t^2(v)}{c_F T^2} - 2\frac{m_t^2(v)}{m_t^2(\phi)}\right]\right]. \tag{2.12}$$

In Eq. (2.10), the numbers of degrees of freedom for SM fields and triplet bosons are given as

$$\begin{aligned} &n_h = 1, \quad n_G = 3, \quad n_S = 2, \quad n_t = 12, \\ &n_{W_L} = n_{Z_L} = n_{\gamma_L} = 1, \quad n_{W_T} = n_{Z_T} = n_{\gamma_T} = 2, \end{aligned} \tag{2.13}$$

while the coefficients c_B and c_F used in Eqs. (2.11) and (2.12) are defined by $\log c_B = 3.9076$ and $\log c_F = 1.1350$, respectively. The Debye masses used in Eq. (2.11)—$\mathcal{M}_i^2(\phi)$ for $i = h, G, T, W_L, W_T, Z_T, \gamma_T$—are as follows:

$$\mathcal{M}_i^2 = m_i^2(\phi) + \Pi_i(\phi,T), \tag{2.14}$$

where $m_i^2(\phi)$ are the field-dependent masses and $\Pi_i(\phi,T)$ are the self-energy contributions given by

$$\begin{aligned} \Pi_h(\phi,T) &= \left(\frac{3g_2+g_1}{16} + \frac{\lambda_1}{2} + \frac{y_t^2}{4} + \frac{\lambda_{hs}}{12}\right)T^2, \\ \Pi_G(\phi,T) &= \left(\frac{3g_2+g_1}{16} + \frac{\lambda_1}{2} + \frac{y_t^2}{4} + \frac{\lambda_{hs}}{12}\right)T^2, \\ \Pi_T(\phi,T) &= \frac{2\lambda_s+\lambda_{hs}}{6}T^2, \\ \Pi_{W_L}(\phi,T) &= \frac{11}{6}g^2T^2, \\ \Pi_{W_T}(\phi,T) &= \Pi_{Z_T}(\Phi,T) = \Pi_{\gamma_T} = 0. \end{aligned} \tag{2.15}$$

Here, the self-energy contribution to the transverse component of gauge bosons W_T, Z_T, and γ_T is zero, and only the longitudinal components get the self-energy contribution. The Debye mass expressions for Z_L and γ_L are written as follows:

$$\mathcal{M}^2_{Z_L} = \frac{1}{2}\left[m^2_Z(\phi) + \frac{11}{6}\frac{g_2}{\cos^2\theta_W}T^2 + \Delta(\phi,T)\right],$$
$$\mathcal{M}^2_{\gamma_L} = \frac{1}{2}\left[m^2_Z(\phi) + \frac{11}{6}\frac{g_2}{\cos^2\theta_W}T^2 - \Delta(\phi,T)\right], \quad (2.16)$$

where Δ is given as

$$\Delta^2(\phi,T) = m^4_Z(\phi) + \frac{11}{3}\frac{g_2\cos^2 2\theta_W}{\cos^2\theta_W} \times \left[M^2_Z(\phi) + \frac{11}{12}\frac{g_2}{\cos^2\theta_W}T^2\right]T^2. \quad (2.17)$$

Now, after getting the full one-loop effective potential including thermal corrections, we can do the complete numerical analysis. To see the effectiveness of plasma screening, we can first include the dominant contribution from the singlet field only by neglecting the contributions from other bosons in the SM. Considering the contribution from singlet only in Eqs. (2.10) and (2.11) and substituting in Eq. (2.9), we get the ϕ-dependent part of the one-loop effective potential as follows:

$$V(\phi) = A(T)\phi^2 + B(T)\phi^4 + C(T)(\phi^2 + K^2(T))^{\frac{3}{2}}. \quad (2.18)$$

Here, the temperature-dependent coefficients are given as

$$A(T) = -\frac{1}{2}\mu^2_T + \frac{1}{4}\left(\frac{\lambda_{hs}}{6} + \frac{y_t^2}{2}\right)T^2,$$
$$B(T) = \frac{1}{4}\lambda_S,$$
$$C(T) = -\left(\frac{\lambda_{hs}}{2}\right)^{\frac{3}{2}}\frac{T}{6\pi},$$
$$K^2(T) = \frac{(\lambda_{hs}+2\lambda_s)T^2 + 6m^2_S}{3\lambda_{hs}}, \quad (2.19)$$

where

$$\mu^2_T = \mu^2 - \frac{\lambda_{hs}}{16\pi^2}\left\{M^2_S(v) + m^2_S\log\frac{c_B T^2}{m^2_S(v)}\right\} + \frac{3}{8\pi^2}y_t^2 m^2_{\rm top}(v)\log\frac{m^2_{\rm top}(v)}{c_F T^2}, \quad (2.20)$$

$$\lambda_T = \lambda_1 + \frac{\lambda^2_{hs}}{32\pi^2}\log\frac{c_B T^2}{m^2_S(v)} + \frac{3}{16\pi^2}y_t^4\log\frac{m^2_{\rm top}(v)}{c_F T^2}. \quad (2.21)$$

It is clear from Eq. (2.18) that $\phi = 0$ is the local minima at a very earlier epoch, if $A(T) > 0$, which leads to the following constraint:

$$-\frac{1}{2}\mu^2_T + \frac{1}{4}\left(\frac{\lambda_{hs}}{6} + \frac{y_t^2}{2}\right) > 0. \quad (2.22)$$

After electroweak (EW) symmetry breaking, $\phi = 0$ is the maxima, and we can find an epoch in between, where a particular temperature T_2 is defined by demanding $V''(0) = 0$. This will give a constraint as follows:

$$4A^2 + 9C^2K^2 = 0. \quad (2.23)$$

The $\phi = 0$ is still the minimum above this temperature, i.e., $T > T_2$, but there exist another maximum and minima at $\phi_-(T)$ and $\phi_+(T)$, respectively [84]. This can be calculated by putting $V'(\phi) = 0$ and demanding that $\phi \neq 0$, which leads to

$$\phi_\pm(T) = \frac{1}{32B^2}\Big(9C^2 - 16AB \pm |C|\sqrt{9C^2 + 32(2B^2K^2 - AB)}\Big). \quad (2.24)$$

These two extrema can merge, resulting in $\phi_-(T) = \phi_+(T)$ at a particular temperature T_1 which is higher than T_2 but lower than the symmetric temperature (T). The $\phi_-(T) = \phi_+(T)$ condition from Eq. (2.24) implies

$$9C^2 + 32(2B^2K^2 - AB) = 0. \quad (2.25)$$

Using the set of equations from Eqs. (2.19)–(2.25), T_1 and T_2 are determined as

$$T_1^2 = \frac{2\lambda_{T_1}(\lambda_{hs}\mu^2_{T_1} + 2\lambda_{T_1}m^2_S)}{\lambda_{hs}\left((\frac{\lambda_{hs}}{6} + \frac{y_t^2}{2})\lambda_{T_1} - \frac{\lambda^3_{hs}}{64\pi^2} - \frac{2\lambda^2_{T1}}{3\lambda_{hs}}(\lambda_{hs} + 2\lambda_s)\right)}, \quad (2.26)$$

$$T_2^2 = \frac{1}{2\alpha}\left(\Lambda^2(T2) + \sqrt{\Lambda^4(T2) - 16\alpha\mu^4_{T2}}\right), \quad (2.27)$$

respectively, where

$$\alpha = \left(\frac{\lambda_{hs}}{6} + \frac{y_t^2}{2}\right)^2 - \frac{1}{24\pi^2}\lambda^2_{hs}(\lambda_{hs} + 2\lambda_s),$$
$$\Lambda^2(T) = \frac{1}{4\pi^2}\lambda^2_{hs}m^2_S + 4\left(\frac{\lambda_{hs}}{6} + \frac{y_t^2}{2}\right)\mu^2_T. \quad (2.28)$$

III. CALCULATION OF FINITE TEMPERATURE POTENTIAL FOR INERT TRIPLET SCENARIO

We extend the SM with a $Y = 0$ (hypercharge = 0) real $SU(2)$ triplet which is odd under Z_2 symmetry. The SM Higgs doublet H as given below transforms under Z_2 as

$H \to H$, whereas the triplet T goes to $-T$. The triplet has one complex charged component $T^{\pm}$ and one neutral component T_0 as shown below. Being Z_2, the neutral component of the triplet T_0 becomes the dark matter candidate. The detailed tree-level mass spectrum and zero temperature vacuum stability analysis are given in Ref. [12]. The corresponding scalar potential is given by

$$V = -\mu^2 H^\dagger H + m_T^2 \mathrm{Tr}(T^\dagger T) + \lambda_1 |H^\dagger H|^2 + \lambda_t (\mathrm{Tr}|T^\dagger T|)^2 + \lambda_{ht} H^\dagger H \mathrm{Tr}(T^\dagger T),$$
$$H = \begin{pmatrix} G^+ \\ \frac{1}{\sqrt{2}}(\phi + h) + iG^0 \end{pmatrix}, \quad T = \frac{1}{2}\begin{pmatrix} T_0 & \sqrt{2}T^+ \\ \sqrt{2}T^- & -T_0 \end{pmatrix}, \tag{3.1}$$

where the neutral component of SM Higgs doublet H, given by ϕ, acts as the background field. However, the field-dependent masses which contribute to the effective potential in the SM include Higgs field h, Goldstone bosons G^0, the gauge bosons ($W^{\pm}$ and Z boson), and the dominant top quark. The field-dependent mass expressions contributing to the effective potential from the SM are calculated as follows:

$$M_h^2(\phi) = 3\lambda_1\phi^2 - \mu^2, \qquad M_{G^0}^2 = \lambda_1\phi^2 - \mu^2,$$
$$M_W^2(\phi) = \frac{g_2}{4}\phi^2, \qquad M_Z^2(\phi) = \frac{(g_2+g_1)}{4}\phi^2,$$
$$M_t^2(\phi) = \frac{y_t^2}{2}\phi^2, \tag{3.2}$$

where M_t is the top-quark mass. As the triplet does not get a VEV, the field-dependent masses for the triplet will be in terms of SM background field ϕ only. The neutral component T_0 and charged component $T^{\pm}$ both will contribute to the effective potential as we present their field-dependent masses:

$$M_{T_0}^2(\phi) = m_T^2 + \frac{\lambda_{ht}}{2}\phi^2,$$
$$M_{T^{\pm}}^2(\phi) = m_T^2 + \frac{\lambda_{ht}}{2}\phi^2. \tag{3.3}$$

In this scenario, the one-loop contributions from bosons are given as

$$\Delta V_B = \sum_{i=h,G,W_L,Z_L,\gamma_L,W_T,Z_T,\gamma_T,T} n_i \Delta V_i, \tag{3.4}$$

where $G \in \{G^0, G^{\pm}\}$, $T \in \{T_0, T^{\pm}\}$, W_L, Z_L, γ_L, W_T, Z_T, and γ_T are defined as the longitudinal and transverse components for gauge bosons $W^{\pm}$ and Z and photon γ, and ΔV_i is given below:

$$\Delta V_i = \frac{m_i^2(\phi)T^2}{24} - \frac{\mathcal{M}_i^3(\phi)T}{12\pi} - \frac{m_i^4(\phi)}{64\pi^2} \times \left[\log\frac{m_i^2(v)}{c_B T^2} - 2\frac{m_i^2(v)}{m_i^2(\phi)} + \delta_{iG}\log\frac{m_h^2(v)}{m_i^2(v)}\right]. \tag{3.5}$$

In Eq. (3.4), the numbers of degrees of freedom for SM fields and triplet bosons are given as

$$n_h = 1, \qquad n_G = 3, \qquad n_T = 3, \qquad n_t = 12,$$
$$n_{W_L} = n_{Z_L} = n_{\gamma_L} = 1, \qquad n_{W_T} = n_{Z_T} = n_{\gamma_T} = 2. \tag{3.6}$$

The Debye masses used in Eq. (3.5) for the inert triplet scenario—$\mathcal{M}_i^2(\phi)$ for $i = h, G, T, W_L, W_T, Z_T, \gamma_T$—are as follows:

$$\mathcal{M}_i^2 = m_i^2(\phi) + \Pi_i(\phi, T), \tag{3.7}$$

where the field-dependent masses $m_i^2(\phi)$ and the self-energy contributions $\Pi_i(\phi, T)$ are given by

$$\Pi_h(\phi,T) = \left(\frac{3g_2+g_1}{16} + \frac{\lambda_1}{2} + \frac{y_t^2}{4} + \frac{\lambda_{ht}}{12}\right)T^2,$$
$$\Pi_G(\phi,T) = \left(\frac{3g_2+g_1}{16} + \frac{\lambda_1}{2} + \frac{y_t^2}{4} + \frac{\lambda_{ht}}{12}\right)T^2,$$
$$\Pi_T(\phi,T) = \frac{2\lambda_t + \lambda_{ht}}{6}T^2,$$
$$\Pi_{W_L}(\phi,T) = \frac{11}{6}g^2T^2,$$
$$\Pi_{W_T}(\phi,T) = \Pi_{Z_T}(\Phi,T) = \Pi_{\gamma_T} = 0. \tag{3.8}$$

Similar to the previous scenario, only the longitudinal components get the self-energy contribution, while the self-energy contribution to the transverse component of gauge bosons W_T, Z_T, and γ_T is zero. The Debye mass expressions for Z_L and γ_L are the same as earlier and are written as follows:

$$\mathcal{M}_{Z_L}^2 = \frac{1}{2}\left[m_Z^2(\phi) + \frac{11}{6}\frac{g_2}{\cos^2\theta_W}T^2 + \Delta(\phi,T)\right],$$
$$\mathcal{M}_{\gamma_L}^2 = \frac{1}{2}\left[m_Z^2(\phi) + \frac{11}{6}\frac{g_2}{\cos^2\theta_W}T^2 - \Delta(\phi,T)\right], \tag{3.9}$$

where Δ is given as

$$\Delta^2(\phi,T) = m_Z^4(\phi) + \frac{11}{3}\frac{g_2\cos^2 2\theta_W}{\cos^2\theta_W} \times \left[M_Z^2(\phi) + \frac{11}{12}\frac{g_2}{\cos^2\theta_W}T^2\right]T^2. \tag{3.10}$$

Here, the temperature-dependent coefficients are now given as

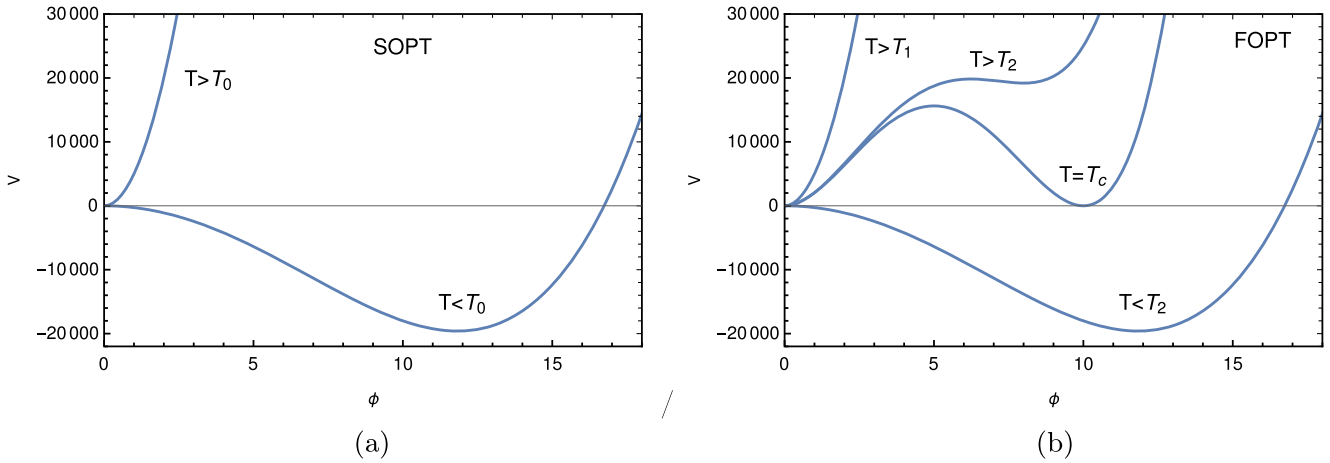

FIG. 1. (a) describes a second-order phase transition, and (b) shows the steps of a first-order phase transition.

$$A(T) = -\frac{1}{2}\mu_T^2 + \frac{1}{4}\left(\frac{\lambda_{ht}}{4} + \frac{y_t^2}{2}\right)T^2,$$
$$B(T) = \frac{1}{4}\lambda_T,$$
$$C(T) = -\left(\frac{\lambda_{ht}}{2}\right)^{\frac{3}{2}}\frac{T}{4\pi},$$
$$K^2(T) = \frac{(2\lambda_{ht} + 4\lambda_t)T^2 + 6m_T^2}{3\lambda_{ht}}, \tag{3.11}$$

where

$$\mu_T^2 = \mu^2 - \frac{3\lambda_{ht}}{32\pi^2}\left\{\sum_{i=T_0,T^\pm} m_i^2(v) + m_T^2 \sum_{i=T_0,T^\pm} \log\frac{c_B T^2}{m_i^2(v)}\right\} + \frac{3}{8\pi^2}y_t^2 m_{\rm top}^2(v)\log\frac{m_{\rm top}^2(v)}{c_F T^2}, \tag{3.12}$$

$$\lambda_T = \lambda_1 + \frac{3\lambda_{ht}^2}{64\pi^2}\log\frac{c_B T^2}{m_T^2(v)} + \frac{3}{16\pi^2}y_t^4\log\frac{m_{\rm top}^2(v)}{c_F T^2}. \tag{3.13}$$

It is clear from Eq. (3.11) that, at a very earlier epoch, $\phi = 0$ is the local minima if $A(T) > 0$, which leads to the following condition:

$$-\frac{1}{2}\mu_T^2 + \frac{1}{4}\left(\frac{\lambda_{ht}}{4} + \frac{y_t^2}{2}\right) > 0. \tag{3.14}$$

After symmetry breaking, $\phi = 0$ will be maxima, and in between we can find an epoch where we can define a particular temperature T_2 by demanding $V''(0) = 0$. This will give a condition as follows:

$$4A^2 + 9C^2K^2 = 0. \tag{3.15}$$

If we go above this temperature, i.e., $T > T_2$, then $\phi = 0$ is still the minimum, but there exist other maxima at $\phi_-(T)$ and minima at $\phi_+(T)$, respectively [84]. This can be achieved by putting $V'(\phi) = 0$ and demanding $\phi \neq 0$, that give

$$\phi_\pm(T) = \frac{1}{32B^2}\left(9C^2 - 16AB \pm |C|\sqrt{9C^2 + 32(2B^2K^2 - AB)}\right). \tag{3.16}$$

At temperatures higher than T_2 but lower than the symmetric temperature (T), these two extrema can merge, resulting in $\phi_-(T) = \phi_+(T)$, which is defined as T_1. The condition for $\phi_-(T) = \phi_+(T)$ from Eq. (3.16) implies

$$9C^2 + 32(2B^2K^2 - AB) = 0. \tag{3.17}$$

Just to remind ourselves, temperatures higher than T_1, i.e., $T > T_1$, which designates the symmetric phase, have just one minimum, i.e., $\phi = 0$. Figure 1(b) shows the shapes of the potential at different thermal epochs. We shall see that these transitions can lead to first-order phase transitions as compared to the smooth second-order phase transition as shown in Fig. 1(a).

For $T < T_2$, $\phi = 0$ is the maximum, and there exists a minimum at $\phi \neq 0$ which evolves toward the zero temperature minimum. Using the set of equations from Eqs. (3.11)–(3.17), we determine T_1 and T_2:

$$T_1^2 = \frac{6144\pi^2\lambda_{T_1}(\lambda_{ht}\mu_{T_1}^2 + 2\lambda_{T_1}m_T^2)}{\lambda_{ht}\left(3072\pi^2(\frac{\lambda_{ht}}{4} + \frac{y_t^2}{2})\lambda_{T_1} - 27\lambda_{ht}^3 - \frac{2048\pi^2\lambda_{T1}^2}{\lambda_{ht}}(2\lambda_{ht} + 4\lambda_t)\right)}, \tag{3.18}$$

$$T_2^2 = \frac{1}{\alpha}\left(\Lambda^2(T2) + \sqrt{\Lambda^4(T2) - 65536\alpha\mu_{T2}^4}\right), \tag{3.19}$$

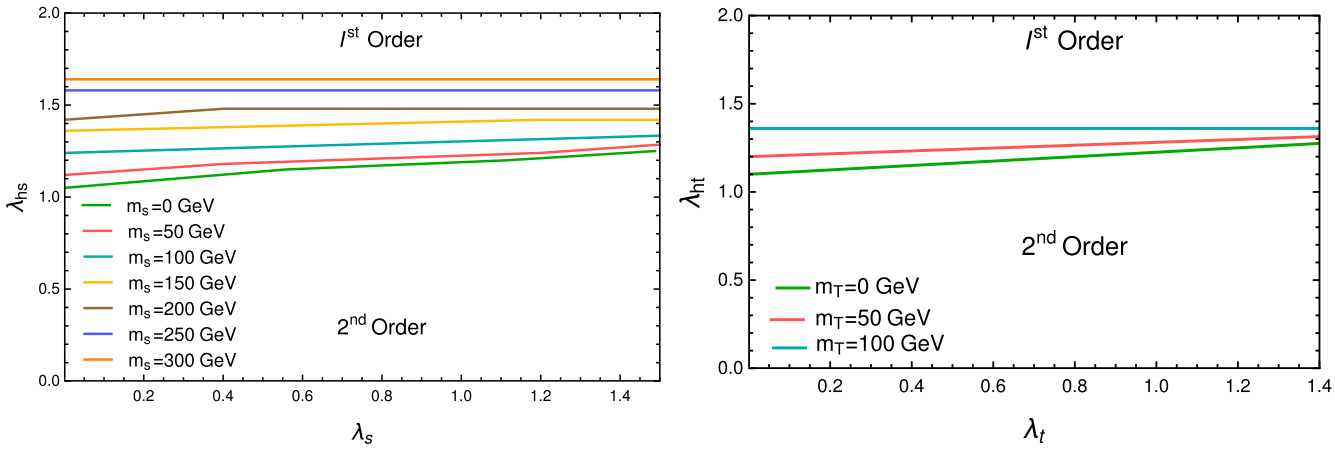

(a) Singlet (b) Triplet

FIG. 2. Plot for the condition $T_1 = T_2$ by varying parameters λ_s/λ_t vs $\lambda_{hs}/\lambda_{ht}$ for the singlet and triplet, respectively. The mass parameter m_S/m_T is varied from 0 to 300 and 0 to 100 GeV with a gap of 50 GeV for the singlet and triplet, respectively. We considered the current experimental values $m_h = 125.5$ GeV and $m_t = 173.2$ GeV. The region above condition $T_1 = T_2$ corresponds to first order and below region for a second-order phase transition. The lower green curve is for $m_S/m_T = 0$ GeV, and the upper one is for $m_S/m_T = 300/100$ GeV with a gap of 50 GeV in the case of the singlet and triplet, respectively.

where

$$\alpha = \left(\frac{\lambda_{ht}}{4} + \frac{y_t^2}{2}\right) - \frac{3}{128\pi^2}\lambda_{ht}^2(2\lambda_{ht} + 4\lambda_t),$$
$$\Lambda^2(T) = 9\lambda_{ht}^2 m_T^2 + 256\left(\frac{\lambda_{ht}}{4} + \frac{y_t^2}{2}\right)\mu_T^2. \quad (3.20)$$

From temperature T_1 and T_2, we can get an idea about the nature of the phase transition. The condition when $T_1 = T_2$ for a particular value of parameters $(\lambda_{ht}, \lambda_t, m_t)$, the nature of the phase transition becomes second order to first order. The first-order phase transition happens via bubble nucleation, when the bubbles of a broken phase start nucleating in the sea of a symmetric phase. This process requires $T_1 > T_2$, when at lower temperature T_2, $\phi = 0$ is the maximum and there exists a deeper $\phi \neq 0$ minimum. While for $T_1 < T_2$, at lower temperature T_1 there is no second minimum deeper than $\phi = 0$, and this gives a second-order phase transition. We considered only the direct one-step transitions from EW symmetric and broken minima. There is also a two-step phase transition possible in a Z_2 symmetric scenario, where the electroweak phase transition proceeds by the spontaneous breaking of the Z_2 symmetry.[2] In the following subsection, we investigate such an effect of Higgs quartic coupling and bare masses of the extra scalars in determining the order of phase transition.

[2]The spontaneous breakdown of Z_2 symmetry gives rise to the domain wall problem, and Z_2 breaking transition is expected to be of second order but not possible to verify within the perturbative effective theory [98].

A. Effect of scalar quartic couplings in phase transition

Here, we explore the dependency of the scalar quartic couplings by presenting $T_1 = T_2$ lines in $\lambda_t - \lambda_{ht}$ plane to segregate regions of first- and second-order phase transition. For a comparison with the complex singlet, we consider the potential of a complex singlet (S) extended SM as given in Ref. [84], where the Higgs-singlet quartic coupling λ_{hs}, λ_s is the self-quartic coupling for the singlet and $m_S = M$ is the bare mass term for the singlet. The nature of phase transition is discussed in Fig. 2 by varying the parameters λ_s/λ_t vs $\lambda_{hs}/\lambda_{ht}$ for the singlet and triplet, respectively. The colored lines correspond to the condition $T_1 = T_2$ for different values of mass parameter, which defines the crossover from first-order to second-order phase transition. The region above the $T_1 = T_2$ condition is first order and below one is second order. For this analysis, we considered the current experimental values $m_h = 125.5$ GeV and $m_t = 173.2$ GeV, respectively [99]. The mass parameters m_S/m_T are varied from 0 to 300 and 0 to 100 GeV with a gap of 50 GeV for the singlet and triplet, respectively. The lower lines denote $m_S/m_T = 0$ GeV, and the uppermost lines correspond to 300 and 100 GeV for the singlet and triplet case, respectively. It is evident from both Figs. 2(a) and 2(b) that, as we enhance the value of the mass parameter m_S/m_T, the required Higgs quartic couplings $\lambda_{hs}/\lambda_{ht}$ for $T_1 = T_2$ are also enhanced; i.e., the first-order phase transition now needs higher quartic couplings. The effect of self-quartic coupling is very minimal and reduces further as we increase the bare mass parameter.

In Sec. IV, we analyze both singlet and triplet scenarios considering all the bosonic degrees of freedom, coupling constants within the perturbativity at two loops, and calculating the exact critical temperature T_c.

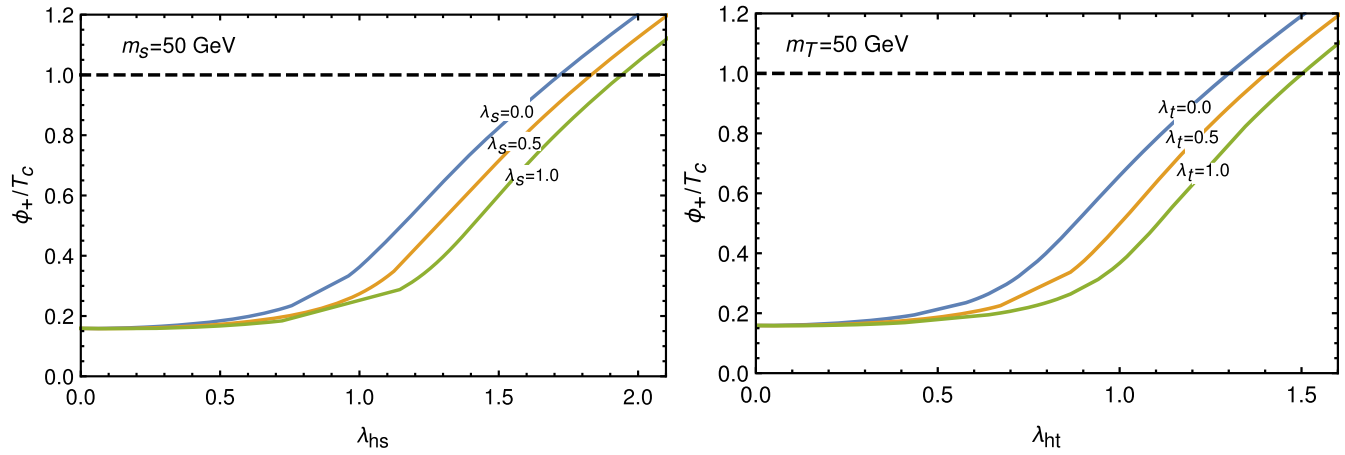

(a) Singlet (b) Triplet

FIG. 3. Variation of $\frac{\phi_+(T_C)}{T_C}$ with respect to the quartic couplings $\lambda_{hs}/\lambda_{ht}$ are shown for the singlet and the triplet, respectively. The self-quartic couplings of the singlet and triplet, i.e., λ_s/λ_t, are assigned three different values 0, 0.5, and 1.0, which are depicted by blue, orange, and green curves, respectively, for fixed mass parameter $m_S/m_T = 50$ GeV with the current experimental values, i.e., $m_h = 125.5$ GeV and $m_t = 173.2$ GeV.

IV. CRITICAL TEMPERATURE AND ELECTROWEAK BARYOGENESIS

In this section, we focus on electroweak baryogenesis and critical temperature during electroweak phase transition caused by a strongly first-order phase transition and the out-of-equilibrium condition. Inside the bubble walls, a net baryon number is generated due to the first-order phase transition as well as the suppressed sphaleron transition. Such B-violating interactions inside the bubble walls also achieve the out-of-equilibrium condition, which helps in baryogenesis. The required criteria for the strongly first-order phase transition can be defined as follows [100,101]:

$$\frac{\phi_+(T_c)}{T_C} \geq 1, \tag{4.1}$$

where T_C is defined as the critical temperature and $\frac{\phi_+(T_c)}{T_C}$ is the parameter which defines the strength of the phase transition. At critical temperature, different two minima of the potential are degenerate, i.e., the same depth, and such a condition defines the critical temperature as

$$V(0;T_C) = V(\Phi_+(T_C);T_C), \tag{4.2}$$

where $V(0;T_C)$ is the potential at $\phi = 0$ minima and $V(\Phi_+(T_C);T_C)$ is the second minima at ϕ_+. In order to calculate $\frac{\phi_+(T_c)}{T_C}$, we take the contributions from all the bosons, i.e., the SM plus the triplet Higgs boson. The variation of $\frac{\phi_+(T_C)}{T_C}$ with respect to the quartic coupling $\lambda_{hs}/\lambda_{ht}$ is considered for $m_S/m_T = 50$ GeV in Fig. 3 for the singlet and the triplet scenarios, respectively. Here, self-quartic couplings λ_s/λ_t are set to 0, 0.5, and 1.0, which are delineated by blue, orange, and green curves, respectively, and with the current experimental values of $m_h = 125.5$ GeV and $m_t = 173.2$ GeV.

For lower values of $\lambda_{hs}/\lambda_{ht}$, the dominant contributions are mainly from the SM fields. For the singlet case [Fig. 3(a)], as we cross $\lambda_{hs} \gtrsim 1$ the effect of the singlet field starts showing up, and for $\lambda_{hs} \gtrsim 1.65$, we attain regions with $\frac{\phi_+(T_c)}{T_C} > 1$. On the contrary, due to more degrees of freedom in the case of the triplet, we see such transitions much earlier, i.e., $\lambda_{ht} \gtrsim 1.3$. One interesting point to note is that with the increase of the self-couplings, i.e., λ_s/λ_t, the $\frac{\phi_+(T_c)}{T_C} > 1$ requires higher values of the interactive Higgs couplings, i.e., $\lambda_{hs}/\lambda_{ht}$.

In Fig. 4, we describe similar variations with respect to $\lambda_{hs/ht}$ for fixed values of self-quartic couplings, i.e., $\lambda_s/\lambda_t = 0$, to maximize $\frac{\phi_+(T_c)}{T_C}$ for the singlet and the triplet, respectively. We also check the dependency over the soft mass parameter m_S/m_T by varying them for 0–400 GeV with a gap of 50 and 1000 GeV, respectively, and are denoted by blue, orange, green, and red curves and so on. It can be seen that as we increase the soft mass m_S/m_T the value of $\frac{\phi_+(T_c)}{T_C}$ decreases for a fixed value of $\lambda_{hs}/\lambda_{ht}$. From Fig. 4(a), we see that after $m_S \geq 350$ GeV getting $\frac{\phi_+(T_c)}{T_C} > 1$ will require $\lambda_{hs} > 3.0$. However, for the triplet scenario in Fig. 4(b), $m_T = 400$ GeV can still give rise to $\frac{\phi_+(T_c)}{T_C} > 1$ with $\lambda_{ht} \geq 2.6$. The couplings $\lambda_{hs}/\lambda_{ht}$ are restricted differently for the singlet and the triplet case from the perturbative unitarity, as we will see in Sec. V. It is clear from Figs. 3 and 4 that the $\frac{\phi_+(T_C)}{T_C}$ parameter is

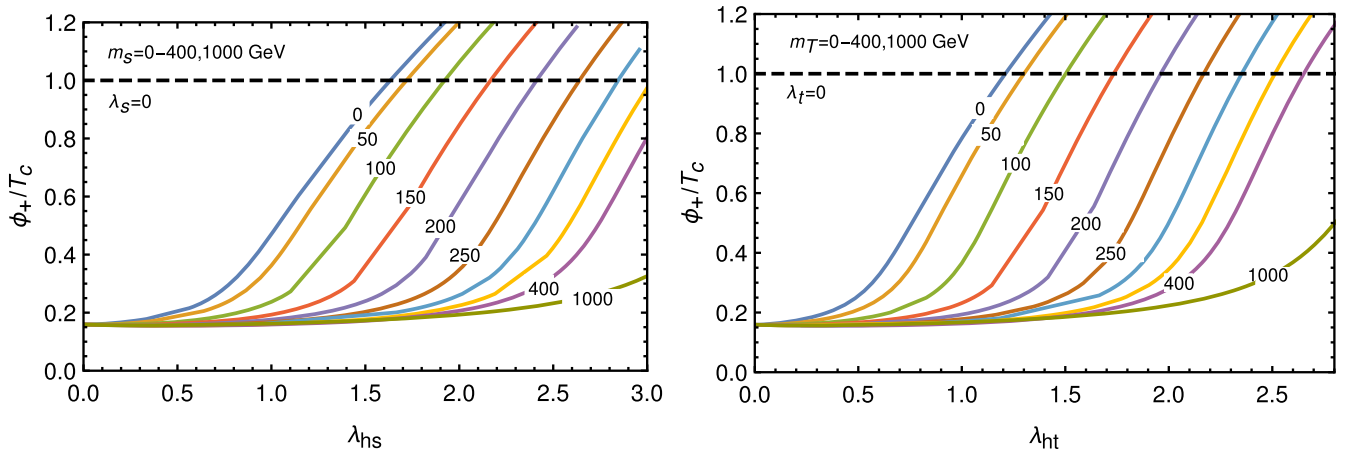

(a) Singlet (b) Triplet

FIG. 4. Variation of $\frac{\phi_+(T_C)}{T_C}$ with quartic coupling $\lambda_{hs}/\lambda_{ht}$ for fixed values of self-quartic couplings $\lambda_s/\lambda_t = 0$ for the singlet and the triplet, respectively. The mass parameter m_S/m_T is varied for 0–400 GeV with a gap of 50 and 1000 GeV, respectively.

maximum for mass parameter $m_S/m_T = 0$ for a fixed value of self-quartic coupling of the singlet or triplet and is also maximum for $\lambda_s/\lambda_t = 0$ for a fixed value of the mass parameter.

V. RG EVOLUTION OF SCALAR QUARTIC COUPLINGS

The renormalized group (RG) evolution of the scalar quartic couplings can give sufficient constraints to the regions responsible for the first-order phase transition from their perturbative unitarity. We explore such a possibility via considering both one- and two-loop beta functions as explained in the following subsections.

A. Constraints from one-loop perturbativity

In this section, we study the RG evolution of the scalar quartic couplings λ_1, λ_t, and λ_{ht} with their one-loop β functions generated by SARAH [102] as given below:

$$\beta_{\lambda_1} = \beta^{\rm SM}_{\lambda_1} + \Delta\beta^{\rm ITM}_{\lambda_1}, \tag{5.1}$$

$$\begin{aligned}\beta^{\rm SM}_{\lambda_1} = \frac{1}{16\pi^2}\Big[&\frac{27}{200}g_1^4 + \frac{9}{20}g_1^2g_2^2 + \frac{9}{8}g_2^4 - \frac{9}{5}g_1^2\lambda_1 - 9g_2^2\lambda_1 \\ &+ 24\lambda_1^2 + 12\lambda_1{\rm Tr}(Y_uY_u^\dagger) + 12\lambda_1{\rm Tr}(Y_dY_d^\dagger) \\ &+ 4\lambda_1{\rm Tr}(Y_eY_e^\dagger) - 6{\rm Tr}(Y_uY_u^\dagger Y_uY_u^\dagger) \\ &- 6{\rm Tr}(Y_dY_d^\dagger Y_dY_d^\dagger) - 2{\rm Tr}(Y_\ell Y_\ell^\dagger Y_\ell Y_\ell^\dagger)\Big],\end{aligned} \tag{5.2}$$

$$\Delta\beta^{\rm ITM}_{\lambda_1} = 8\lambda_{ht}^2, \tag{5.3}$$

$$\beta_{\lambda_t} = \frac{1}{16\pi^2}\left[-24g_2^2\lambda_t + 88\lambda_t^2 + 8\lambda_{ht}^2 + \frac{3}{2}g_2^4\right], \tag{5.4}$$

$$\begin{aligned}\beta_{\lambda_{ht}} = \frac{1}{6\pi^2}\Big[&\frac{3}{4}g_2^4 - \frac{9}{10}g_1^2\lambda_{ht} - \frac{33}{2}g_2^2\lambda_{ht} + 12\lambda\lambda_{ht} \\ &+ 16\lambda_{ht}^2 + 24\lambda_{ht}\lambda_t + 6y_t^2\lambda_{ht}\Big],\end{aligned} \tag{5.5}$$

where $\Delta\beta^{\rm ITM}_\lambda$ is the additional contribution to SM β_λ from the inert triplet. Since $\frac{\phi_+(T_C)}{T_C}$ is maximum, both mass parameters m_S/m_T and the self-quartic couplings λ_s/λ_t are zero. We have chosen $\lambda_s/\lambda_t = 0$ at the EW scale for our analysis, and RG evolutions at one and two loops govern the couplings at any other scales. Hence, to maximize $\frac{\phi_+(T_C)}{T_C}$, we choose $\lambda_s/\lambda_t = 0$ at the EW scale for further analysis. One point to note here is that the mass parameter does not enter in the running of quartic couplings; thus, the choice of $\lambda_s/\lambda_t = 0$ is sufficient for perturbative unitarity. To keep the SM Higgs mass around 125.5 GeV, we keep the SM quartic coupling $\lambda_1 = 0.13$ at the EW scale. In Table I, Λ designates the perturbative scale where any of the coupling crosses the perturbativity (4π). We fix quartic

TABLE I. Maximum allowed values of λ_{hs} and λ_{ht} from the perturbativity at one loop for the top mass, i.e., $m_t = 173.2$ GeV, and for the Higgs boson mass $m_h = 125.5$ GeV.

	$\lambda_{hs} = \lambda_{hs}^{\rm max}$	$\lambda_{ht} = \lambda_{ht}^{\rm max}$
	m_t (GeV)	m_t (GeV)
Λ (GeV)	173.2	173.2
10^4	1.6545	1.3710
10^6	0.7290	0.7067
10^8	0.5120	0.4873
10^{11}	0.4780	0.3477
10^{16}	0.3090	0.2490
10^{19}	0.2370	0.2180

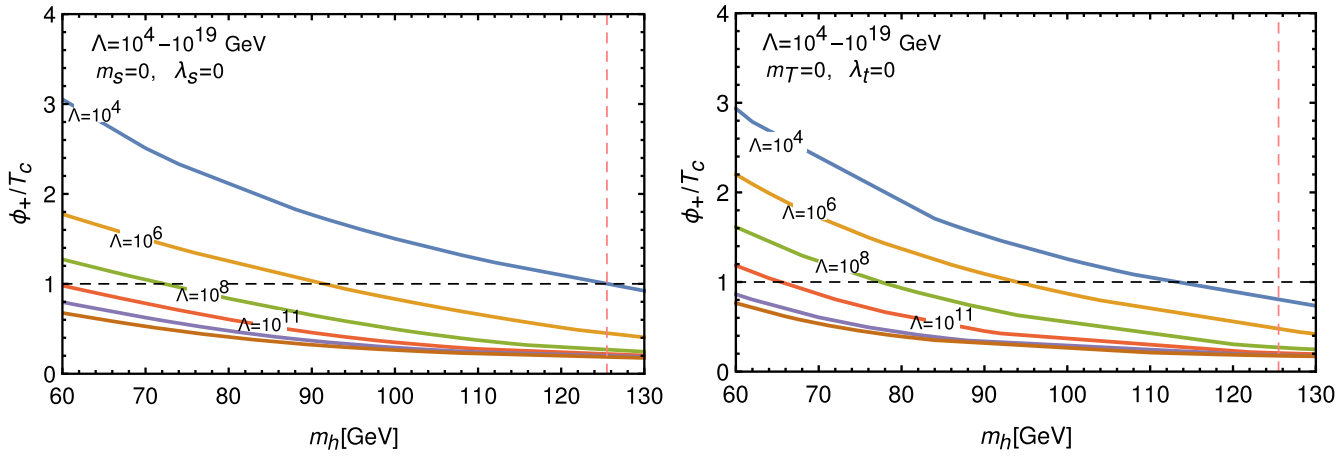

(a) Singlet (b) Triplet

FIG. 5. Variation of $\frac{\phi_+(T_C)}{T_C}$ with respect to the Higgs boson mass m_h in GeV for fixed initial values of $\lambda_{hs}^{\max}/\lambda_{ht}^{\max}$ at different perturbative scales as shown in Table I. The mass parameter m_S/m_T and self-quartic couplings λ_s/λ_t are chosen to be zero to maximize the strength of the phase transition with $m_t = 173.2$ GeV.

couplings $\lambda_{hs}/\lambda_{ht}$ at the EW scale and check the perturbative unitarity till a particular scale Λ. To show the effect of the top-quark mass, we present the maximum values of the quartic couplings at the EW scale allowed for two different top-quark masses, i.e., 120.0 and 173.2 GeV, respectively, for the singlet and the triplet scenarios. We see that, due to larger scalar degrees of freedom, the triplet scenario gets more restriction than the singlet one. For example, considering Planck-scale perturbativity, the singlet can have a $\lambda_{hs}^{\max} = 0.237(0.248)$, whereas the triplet scenario gets $\lambda_{ht}^{\max} = 0.2180(0.2202)$ for $m_t = 173.2(120.0)$ GeV. For lower top mass, the large negative contribution from the top quark slows down the running of scalar quartic coupling toward the perturbative limit. It can also be observed that, as we demand a lower scale for the perturbativity, higher values of $\lambda_{hs}^{\max}/\lambda_{ht}^{\max}$ at the EW scale can be attained. In the next subsection, we discuss such effects at the two-loop level.

In Fig. 5, we present the variation of $\frac{\phi_+(T_C)}{T_C}$, i.e., the strength of the phase transition with the SM Higgs boson mass for the singlet and the triplet scenario, where we consider $\lambda_{hs}^{\max}/\lambda_{ht}^{\max}$ as given in Table I for a given scale Λ. Figure 5(a) depicts the situation for the complex singlet extension, where it is evident that higher values of $\frac{\phi_+(T_C)}{T_C}$ are possible with a lower perturbativity scale and lower SM Higgs boson mass. It is interesting to note that $m_h = 125.5$ GeV and $\frac{\phi_+(T_C)}{T_C} > 1$ is not possible even for the perturbative scale $\Lambda = 10^6$ GeV, and only $\Lambda = 10^4$ GeV can barely satisfy the condition of the first-order phase transition. The values of $\lambda_{hs}^{\max}/\lambda_{ht}^{\max}$ are similar for $\Lambda = 10^6$ GeV; however, due to more degrees of freedom, the triplet scenario guarantees larger $\frac{\phi_+(T_C)}{T_C}$ for a given m_h. The perturbative scale $\Lambda = 10^4$ GeV allows larger $\lambda_{hs}^{\max}$ compared to $\lambda_{ht}^{\max}$, resulting in an enhancement of $\frac{\phi_+(T_C)}{T_C}$ in favor of the singlet, and it barely makes it for $\frac{\phi_+(T_C)}{T_C} \simeq 1$ at $m_h = 125.5$ GeV; however, the triplet case fails to achieve that at one-loop level.

The dependence of the top-quark mass is explored in Fig. 6 for the variation of $\frac{\phi_+(T_C)}{T_C}$ with the Higgs boson mass for the choices of the mass parameters m_S/m_T and self-quartic couplings λ_s/λ_t equal to zero for the perturbative scale $\Lambda = 10^6$ GeV. The maximum allowed quartic couplings $\lambda_{hs}^{\max}/\lambda_{ht}^{\max}$ are estimated using $m_t = 120.0$ and 173.2 GeV and $m_h = 125.5$ GeV at the electroweak scale for the perturbative scale of $\Lambda = 10^6$ GeV, and $m_t = 173.2$ values are described in Table I. The blue and orange curves present $m_t = 120.0$ and 173.2 GeV cases, respectively, for the singlet [Fig. 6(a)] and triplet scenarios [Fig. 6(b)]. The maximum allowed quartic coupling $\lambda_{ht}^{\max}$ is lower for the triplet due to more degrees of freedom, which catalyzes an early perturbative restriction. Nevertheless, the slight decrement of $\lambda_{ht}^{\max}$ compared to $\lambda_{hs}^{\max}$ is overpowered by more degrees of freedom giving little higher values of the $\frac{\phi_+(T_C)}{T_C}$ for a given m_h. The upper bound on the Higgs mass to avoid baryon asymmetry washout, i.e., $\frac{\phi_+(T_C)}{T_C} > 1$, is 91.0 and 93.0 GeV for the singlet and the triplet, respectively. Thus, we can conclude that these upper bounds on the Higgs mass from baryon asymmetry for both cases, considering one-loop perturbativity of the quartic couplings, are not consistent with the current observed experimental Higgs mass of 125.5 GeV.

Before ending the discussion of one-loop perturbativity and moving on to two-loop results, we present the results in a three-dimensional graph in Fig. 7, where we study the variation of $\phi_+(T_c)/T_c$ in the $\lambda_{hs}^{\max}/\lambda_{ht}^{\max} - m_h$ plane.

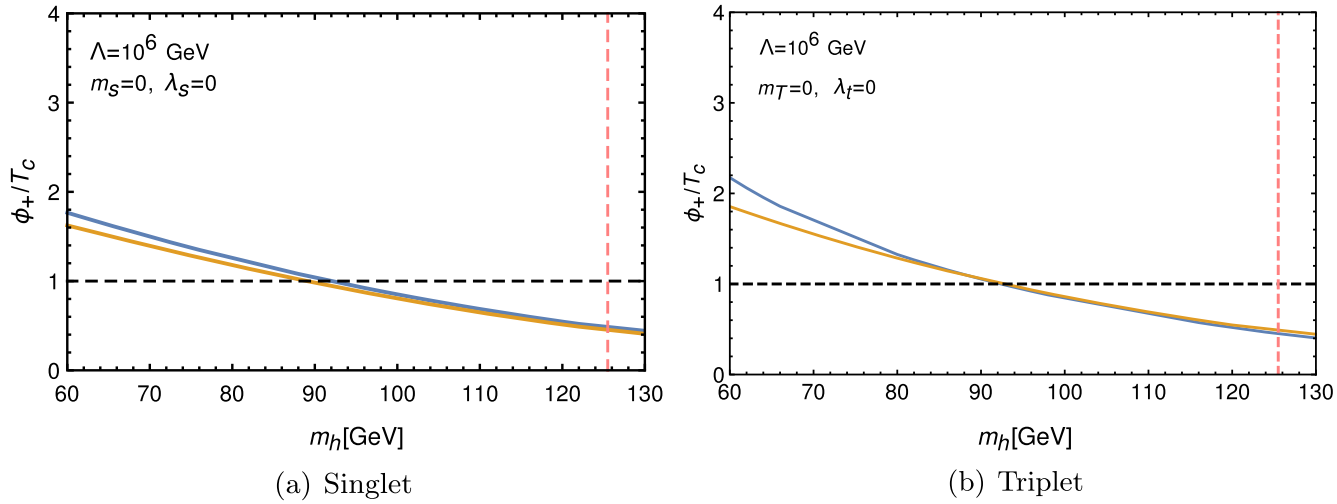

(a) Singlet (b) Triplet

FIG. 6. Variation of $\phi_+(T_c)/T_c$ with Higgs mass m_h for two different values of top mass $m_t = 120.0$ and 173.2 GeV designated by blue and orange curves, respectively, for the perturbative scale of 10^6 GeV.

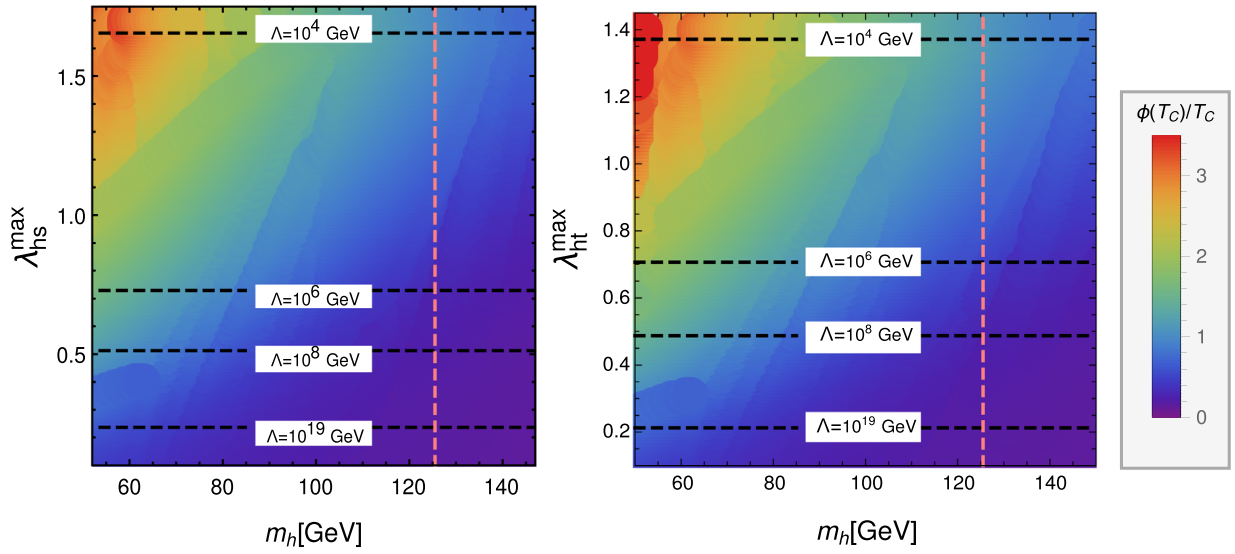

(a) Singlet (b) Triplet

FIG. 7. Variation of $\phi_+(T_c)/T_c$ in the $\lambda_{hs}^{\max}/\lambda_{ht}^{\max} - m_h$ plane, where $\lambda_{hs}^{\max}/\lambda_{ht}^{\max}$ are the maximum allowed values of quartic coupling at different perturbative scales in GeV for the singlet and the triplet scenarios, respectively. The color band from deep blue to red regions signifies $\phi_+(T_c)/T_c$ in 0–3.5 for both scenarios.

The color band of $\phi_+(T_c)/T_c$ from deep blue to red regions signifies $\phi_+(T_c)/T_c$ in 0–3.5 for both scenarios. The self-couplings for the singlet and the triplet and their corresponding soft masses are chosen to be zero in order to enhance $\phi_+(T_c)/T_c$. It is very apparent from Fig. 7 that a much lower perturbative scale Λ and lighter SM Higgs boson are preferred in order to achieve a first-order phase transition, i.e., $\phi_+(T_c)/T_c > 1$. Only for the singlet case can $\Lambda = 10^4$ GeV scale have a first-order phase transition with a SM Higgs boson mass around 125.5 GeV. The choice of zero soft masses in order to have a first-order phase transition for both scenarios may restrict the physical singlet and triplet scalars. However, as we explore in the following subsection, two-loop perturbativity gives a little breather, and such upper limits on the physical singlet and triplet masses are enhanced.

B. Constraints from two-loop perturbativity

For the given values of quartic couplings at the electroweak scale, i.e., λ_1, $\lambda_{hs/ht}$, and $\lambda_{s/t}$, they hit the Landau pole at the same scale considering one-loop RG evolution. Depending on the validity scale of perturbativity, certain constraints come for the maximum electroweak values of

TABLE II. Maximum allowed value of quartic couplings, i.e., $\lambda_{hs}^{\max}/\lambda_{ht}^{\max}$, allowed at the electroweak scale for the perturbativity till Planck scale at two loops, for the singlet and the triplet scenarios.

Λ (GeV)	$\lambda_{hs}^{\max}$	$\lambda_{ht}^{\max}$
10^{19}	4.00	1.95

the couplings, as we have seen in Table I. For example, if we choose the perturbativity scale as the Planck scale, i.e., $\Lambda = 10^{19}$ GeV, $\lambda_{hs}^{\max}$ and $\lambda_{ht}^{\max}$ are restricted to 0.23 and 0.21, respectively, at one-loop level. The slight difference comes due to the variation of λ_t affecting λ_1.

The situation changes a lot as we move to two-loop RG evolution (see Appendix A). Contrary to the one-loop case, here λ_1 hits the Landau pole before $\lambda_{hs/ht}$ and $\lambda_{s/t}$. However, the growth of λ_1 coupling slows down at two loops as compared to one loop, due to the negative contributions, i.e., $-312\lambda_1^3$, $-80\lambda_1\lambda_{ht}^2$, and $-128\lambda_{ht}^3$ as shown in Sec. A 1. Similarly, other quartic couplings, i.e., λ_{ht} and λ_t, also slow down due to some extra negative contributions appearing at two loops (see Sec. A 1). In comparison, the singlet also suffers from the negative contributions of $-312\lambda_1^3$, $-40\lambda_1\lambda_{hs}^2$, and $-32\lambda_{hs}^3$ as can be read from Sec. B 1. However, if we look at the maximum allowed value ($\lambda_{hs}^{\max}/\lambda_{ht}^{\max}$) at the electroweak scale at two-loop level in Table II for the Planck-scale perturbativity, the singlet can access double the value that of the triplet one. This can be understood as the triplet having more positive contributions in terms of $10g_2^4\lambda_{ht}$ and $32g_2^2\lambda_{ht}^2$ in λ_1, which are absent in the singlet one. Thus, the growth of λ_1 in the triplet case is faster, hitting the Landau pole much earlier, as compared to the singlet one. The presence of such extra positive contributions at the two-loop level for the triplet explains the larger difference in $\lambda_{ts}^{\max}$ and $\lambda_{hs}^{\max}$ (see Table II) as compared to one-loop level (see Table I).

In order to examine the situation of the possibility of the first-order phase transition with the perturbativity at the two-loop level, we calculate the maximum allowed values of the quartic couplings, i.e., $\lambda_{hs}^{\max}/\lambda_{ht}^{\max}$, with the Planck-scale perturbativity ($\Lambda = 10^{19}$ GeV) as given in Table II. The slow-growing quartic coupling at two loops compared to one loop enhanced the allowed couplings for $\lambda_{hs}^{\max} = 4.00$ and $\lambda_{ht}^{\max} = 1.95$ at the electroweak scale. These are now enormously amplified compared to the corresponding one-loop values $\lambda_{hs}^{\max} = 0.25670$ and $\lambda_{ht}^{\max} = 0.2180$, which result in higher values of $\phi_+(T_c)/T_c$, strengthening the possibility of a first-order phase transition for both scenarios.

Equipped with relatively larger $\lambda_{hs}^{\max}/\lambda_{ht}^{\max}$ for $\Lambda = 10^{19}$ GeV, we now perform the variation of $\frac{\phi_+(T_C)}{T_C}$ with respect to m_h in Fig. 8, where the scalar self-couplings are chosen to be zero. The mass parameters varied for $m_S(m_T) = 500(100)$, 840(200), and 1000(300) are denoted by blue, orange, and green curves, respectively. The red star in both cases denotes $\frac{\phi_+(T_C)}{T_C} = 1$ and the $m_h = 125.5$ GeV point. Higher mass values diminish the $\frac{\phi_+(T_C)}{T_C}$ and push for a second-order phase transition for both scenarios. However, for the singlet scenario, we see a maximum of $m_S = 840$ GeV can still be consistent with the SM Higgs boson mass as well as a first-order phase transition, whereas, for the triplet scenario, such bounds come for a rather low mass, i.e., $m_T \simeq 193$ GeV. We see an order of magnitude difference in the upper bound on the soft mass parameter in the singlet and the triplet scenarios.

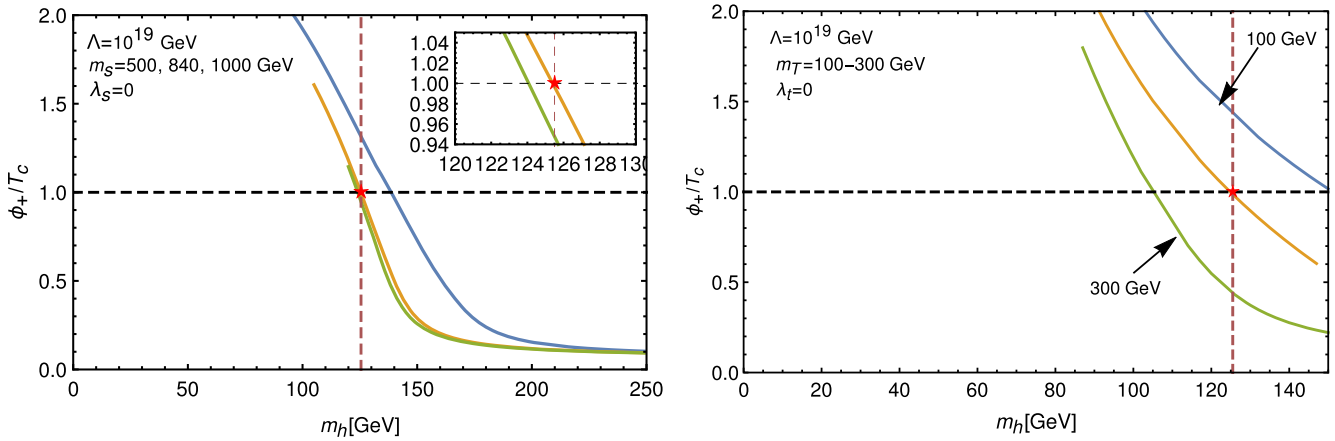

(a) Singlet (b) Triplet

FIG. 8. Variation of $\phi_+(T_c)/T_c$ with respect to the SM Higgs boson mass m_h (in GeV) for the singlet and the triplet scenarios. Three different values of mass parameters for $m_S(m_T) = 500(100)$, 840(200), and 1000(300) are denoted by blue, orange, and green curves, respectively. The quartic couplings $\lambda_{hs}/\lambda_{ht}$ are fixed to their respective $\lambda_{hs}^{\max}/\lambda_{ht}^{\max}$ with the perturbativity at the Planck scale (10^{19} GeV), and the self-couplings are chosen to be zero.

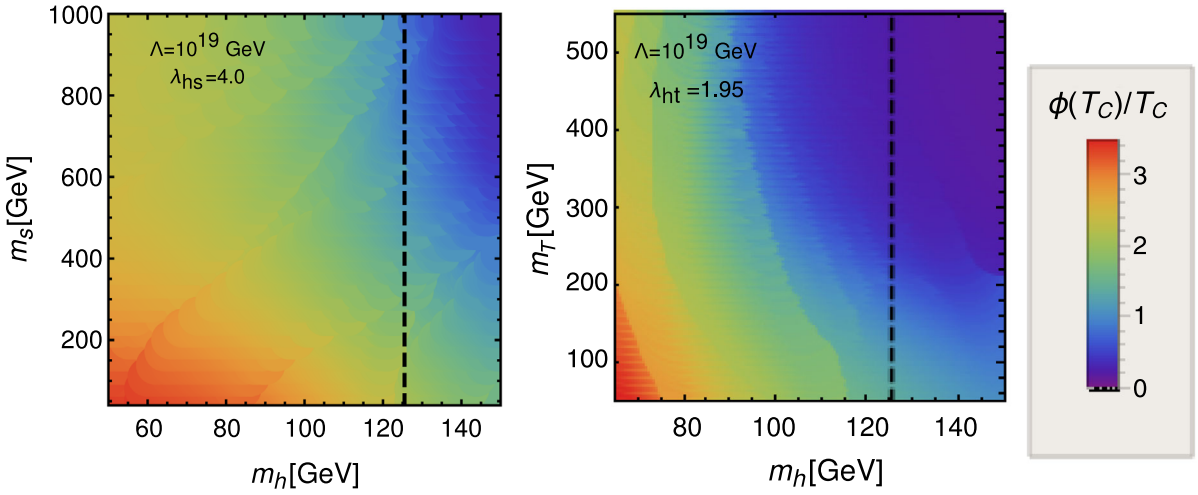

(a) Singlet (b) Triplet

FIG. 9. Variation of $\phi_+(T_c)/T_c$ in $m_S/m_T - m_h$ for the maximum allowed values of quartic coupling $\lambda_{hs}^{\max}/\lambda_{ht}^{\max}$ at the electroweak scale for the perturbativity till Planck scale (10^{19} GeV) for the singlet and the triplet scenarios, respectively. The color band from deep blue to red regions signifies $\phi_+(T_c)/T_c$ in 0–3.5 for both scenarios.

In Fig. 9, we present $\phi_+(T_c)/T_c$ in the $m_S/m_T - m_h$ plane for the maximum allowed values of quartic coupling $\lambda_{hs}^{\max}/\lambda_{ht}^{\max}$ at the electroweak scale for the perturbativity till Planck scale (10^{19} GeV) for the singlet and the triplet scenarios, respectively. The color band from deep blue to red regions signifies $\phi_+(T_c)/T_c$ in 0–3.5 for both scenarios. It is evident that for higher mass values $m_T \geq 193$ GeV in the triplet case stay in the deep blue region for $m_h = 125.5$ GeV, conferring a second-order phase transition. On the contrary, in the singlet case one can obtain regions up to $m_S \simeq 840$ GeV satisfying a first-order phase transition at $m_h = 125.5$ GeV.

C. Two-loop resummed potential

The field-dependent term in the effective potential from one-loop daisy resummation is $\mathcal{O}(g^3)$, but achieving accuracy of $\mathcal{O}(g^4)$ requires two-loop corrections when two-loop β functions are analyzed. The most efficient two-loop contributions are of the form $\phi^2\log(\phi)$, which are induced by the Standard Model weak gauge boson loops [16]. The diagrams contributing to the two-loop potential for the minimal Standard Model are given in Refs. [97,103,104]. In the case of an inert singlet, there is no additional diagram which contributes to the two-loop potential. Therefore, the two-loop correction for the inert singlet comes only from the Standard Model and is given as follows:

$$V_2 \simeq \log\frac{T}{\phi}\frac{\phi^2T^2}{32\pi^2}\left[\frac{51}{16}g_2^4\right]. \tag{5.6}$$

Similarly, in the case of an inert triplet, there are diagrams which give additional contributions to the two-loop potential along with the SM part. The two-loop resummed potential for the inert triplet scenario is given as

$$V_2 \simeq \log\frac{T}{\phi}\frac{\phi^2T^2}{32\pi^2}\left[\frac{51}{16}g_2^4 + \frac{3}{16}g_2^4\right], \tag{5.7}$$

where the first term comes from the SM and the second term comes from the inert triplet.

After adding these two-loop contributions to the full one-loop effective potential, the strength of the phase transition enhances [105,106] in both cases, which actually changes the mass bounds. However, for the singlet one-loop maximum mass required for first-order phase transition $\simeq 909$ GeV, which already decouples and does not alter the phase transition. With inclusion of a two-loop correction, this bound is still consistent with Planck-scale perturbativity and satisfies the Higgs boson mass bound within 1σ uncertainty because of the increase in the strength of the phase transition. Thus, the singlet mass bound still remains the same at the two-loop resummed potential. On the contrary, the effect is visible in the case of the inert triplet, owing to a lower mass bound of $\simeq$310 GeV at one-loop potential. Inclusion of the two-loop resummed potential inflates the mass bound slightly to $\simeq$320 GeV, satisfying the Planck-scale perturbativity and the current experimental Higgs boson mass bound.

VI. DIMENSIONAL REDUCTION

The effective potential at finite temperature has residual scale dependence at $\mathcal{O}(g^4)$. The cancellation of this scale dependence at $\mathcal{O}(g^4)$ requires the inclusion of two-loop thermal masses to bare masses for Higgs, singlet, and triplet, i.e., μ, m_S, and m_T, respectively. The most common

way is to utilize high-temperature dimensional reduction to a three-dimensional effective field theory (3D EFT) in order to derive the full $\mathcal{O}(g^4)$ thermal effective potential. The dimensional reduction technique is a systematic approach required at high temperature to the resummations done order by order in power of couplings [107,108]. The $\mathcal{O}(g^4)$ result for the Z_2-symmetric real scalar theory with the two-loop results has been derived long ago. The one-loop potential to this order reads as

$$V^{g^4}_{\text{thermal}}(v) = \frac{1}{(4\pi)^2}\left[\frac{1}{12}g_2^4T^2v^2\left(\frac{1}{2}\log\left(\frac{M^2(v)+\Pi_T}{T^2}\right)-\frac{3}{8}L_b(\Lambda)-c+\frac{1}{4}\right)\right] + \frac{1}{(4\pi)^2}\left(-\frac{1}{4}g_2^2\mu^2v^2L_b(\Lambda)-\frac{1}{16}g_2^4v^4L_b(\Lambda)\right)+\text{const}, \tag{6.1}$$

where we have introduced the notation using the following:

$$c = -\log\left(\frac{3e^{\gamma/2}A^6}{4\pi}\right) = -0.348723\ldots, \tag{6.2}$$

$$L_b(\Lambda) = 2\log\left(\frac{e^{\gamma}\Lambda}{4\pi T}\right), \tag{6.3}$$

where A is the Glaisher-Kinkelin constant and γ is the Euler-Mascheroni constant. The full two-loop effective potential expression is as follows:

$$V_{\text{thermal}} = TV^{3d}_{\text{eff}} = T\left[\frac{1}{2}\mu_3^2v_3^2+\frac{1}{4!}g_{2,3}^2v_3^4-\frac{1}{3(4\pi)}(M_3^2)^{3/2}+\frac{1}{(4\pi)^2}\left(\frac{1}{8}g_{2,3}^2M_3^2-\frac{1}{24}g_{2,3}^4v_3^2\left[1+2\ln\left(\frac{\mu_3}{3M_3}\right)\right]\right)\right], \tag{6.4}$$

where the one-to-one correspondence between Higgs quartic coupling λ_3 and $g_{2,3}$ is $\lambda_3 = \frac{1}{6}g_{2,3}^2$ and the expressions for two-loop thermal masses are as follows:

$$M_3^2 = \mu_3^2+\frac{1}{2}g_{2,3}^2v_3^2. \tag{6.5}$$

The 3D effective parameters to the same $\mathcal{O}(g^4)$ order are given as

$$g_{2,3}^2 = T\left(g_2^2(\Lambda)-\frac{3}{2(4\pi)^2}g_2^4L_b(\Lambda)\right), \tag{6.6}$$

$$\mu_3^2 = \mu^2(\Lambda)+\frac{1}{24}g_2^2(\Lambda)T^2-\frac{1}{(4\pi)^2}\left(\frac{1}{2}g_2^2\mu^2L_b(\Lambda) + \frac{1}{16}g_2^4T^2L_b(\mu)+\frac{1}{6}g_{2,3}^4\left[c+\ln\left(\frac{3T}{\Lambda_{3d}}\right)\right]\right), \tag{6.7}$$

$$v_3 = \frac{v}{\sqrt{T}}. \tag{6.8}$$

In the next section, we present similar expressions for dimensionally reduced 3D theory for the SM extended with an inert singlet and an inert triplet.

A. Singlet extension

The scalar potential given in Eq. (2.1) for the inert singlet scenario in the dimensionally reduced 3D effective theories (DR3EFTs) is given as

$$V = -\mu_3^2H^\dagger H+m_{S,3}^2S^*S+\lambda_{1,3}|H^\dagger H|^2+\lambda_{s,3}|S^*S|^2 + \lambda_{hs,3}(H^\dagger H)(S^*S). \tag{6.9}$$

Now, the thermal contribution to the self-energy in Eq. (2.15) has the schematic form $\Pi_T \sim g^2T^2$. If we consider the running of the $\Pi_T v^2$ term, the effect is of $\mathcal{O}(g^4T^2v^2)$ which is not canceled by any resummed one-loop or any other one-loop contribution to the effective potential. This cancellation of renormalization scale dependence is canceled only by the inclusion of explicit logarithms of the renormalization scale, which appear only at two-loop level. At high temperature, the order of the running of tree-level parameters is the same as the running of one-loop thermal mass, and this order is also similar to explicit logarithms of the renormalization scale appearing at two-loop order. All three terms are of the order of $\mathcal{O}(g^4T^2)$. The third and the fourth terms in the full two-loop potential at $\mathcal{O}(g^4)$ for 3D theory will include contributions from the bosons and the fermions similar to Eq. (2.10).

Hence, the matching relations for the quartic couplings and the bare masses (which are the tree-level parameters) are computed as follows [98,109]:

$$\lambda_{1,3} = T\left[\lambda_1(\Lambda) + \frac{1}{(4\pi)^2}\left(\frac{2-3L_b}{16}(3g_2^4 + 2g_2^2g_1^2 + g_1^4) + N_cL_f(y_t^4 - 2\lambda_1 y_t^2) + L_b\left(\frac{3}{2}(3g_2^2 + g_1^2)\lambda_1 - 12\lambda_1^2 - \frac{1}{4}\lambda_{hs}\right)\right)\right],$$
$$\lambda_{s,3} = T\left[\lambda_s(\Lambda) - \frac{1}{(4\pi)^2}L_b(\lambda_{hs}^2 + 9\lambda_s^2)\right],$$
$$\lambda_{hs,3} = T\left[\lambda_{hs}(\Lambda) + \frac{\lambda_{hs}}{(4\pi)^2}\left(L_b\left(\frac{3}{4}(3g_2^2 + g_1^2) - 6\lambda_1 - 2\lambda_{hs} - 3\lambda_s\right) - N_cL_f y_t^2\right)\right], \tag{6.10}$$

where

$$L_b = \ln\left(\frac{\Lambda^2}{T^2}\right) - 2[\ln(4\pi) - \gamma], \tag{6.11}$$

$$L_f = L_b + 4\ln 2. \tag{6.12}$$

Here, L_b and L_f are logarithms that arise frequently from one-loop bosonic and fermionic sum integrals with Λ the $\overline{\text{MS}}$ scale and γ the Euler-Mascheroni constant. The expressions for the two-loop mass parameters are computed as follows:

$$\mu_3^2 = (\mu_3^2)_{\text{SM}} + \frac{T^2}{24}\lambda_{hs}(\Lambda) - \frac{L_b}{(4\pi)^2}\left(\frac{1}{2}\lambda_{hs}\mu_S^2(\Lambda)\right) + \frac{1}{(4\pi)^2}\left(\frac{3}{4}(3g_2^2 + g_1^2)L_b - N_cy_t^2L_f\right)\left(\frac{T^2}{24}\lambda_{hs}\right)$$
$$- \frac{T^2}{(4\pi)^2}L_b\lambda_{hs}\left(\frac{1}{4}\lambda_1 + \frac{5}{24}\lambda_{hs} + \frac{1}{8}\lambda_s\right) - \frac{1}{(4\pi)^2}\frac{1}{2}\lambda_{hs,3}^2\left(c + \ln\left(\frac{3T}{\Lambda_{3d}}\right)\right), \tag{6.13}$$

where

$$(\mu_3^2)_{\text{SM}} = -\mu^2(\Lambda) + \frac{T^2}{12}\left(\frac{3}{4}(3g_2^2(\Lambda) + g_1^2(\Lambda)) + N_cy_t^2(\Lambda) + 6\lambda_1(\Lambda)\right) + \frac{\mu^2(\Lambda)}{(4\pi)^2}\left(\left(\frac{3}{4}(3g_2^2 + g_1^2) - 6\lambda_1\right)L_b - N_cy_t^2L_f\right)$$
$$+ \frac{T^2}{(4\pi)^2}\left[\frac{167}{96}g_2^4 + \frac{1}{288}g_1^4 - \frac{3}{16}g_2^2g_1^2 + \frac{(1+3L_b)}{4}\lambda_1(3g_2^2 + g_1^2) + L_b\left(\frac{17}{16}g_2^4 - \frac{5}{48}g_1^4 - \frac{3}{16}g_2^2g_1^2 - 6\lambda_1^2\right)\right.$$
$$+ \frac{1}{T^2}\left(c + \ln\left(\frac{3T}{\Lambda_{3d}}\right)\right)\left(\frac{39}{16}g_{2,3}^4 + 12g_{2,3}^2h_3 - 6h_3^2 + 9g_{2,3}^2\lambda_{1,3} - 12\lambda_{1,3}^2 - \frac{5}{16}g_{1,3}^4 - \frac{9}{8}g_{2,3}^2g_{1,3}^2 - 2h_3'^2 - 3h_3''^2\right.$$
$$\left.+ 3g_{1,3}^2\lambda_{1,3}\right) - \frac{1}{96}(9L_b - 3L_f - 2)\left((N_c+1)g_2^4 + \frac{1}{6}Y_{2f}g_1^4\right)n_f + \frac{N_c}{32}(7L_b - L_f - 2)g_2^2y_t^2$$
$$- \frac{N_c}{4}(3L_b + L_f)\lambda_1y_t^2 + \frac{N_c}{96}((9(L_b - L_f) + 4)Y_\phi^2 - 2(L_b - 4L_f + 3)(Y_q^2 + Y_u^2))g_1^2y_t^2$$
$$\left.- \frac{N_cC_F}{6}(L_b - 4L_f + 3)g_s^2y_t^2 + \frac{N_c}{24}(3L_b - 2(N_c - 3)L_f)y_t^4\right], \tag{6.14}$$

with $C_F = \frac{N_c^2-1}{2N_c} = \frac{4}{3}$ and $c \sim -0.348723$, is the fundamental quadratic Casimir of $SU(3)$. And the two-loop mass parameter for the singlet is given as

$$m_{S,3}^2 = m_S^2(\Lambda) + T^2\left(\frac{1}{6}\lambda_{hs}(\Lambda) + \frac{1}{4}\lambda_s(\Lambda)\right) - \frac{L_b}{(4\pi)^2}(2\lambda_{hs}\mu^2 + 3\lambda_sm_S^2) + \frac{1}{(4\pi)^2}((3g_{2,3}^2 + g_{1,3}^2)\lambda_{hs,3} - 2\lambda_{hs,3}^2 - 6\lambda_{s,3}^2)$$
$$\left(c + \ln\left(\frac{3T}{\Lambda_{3d}}\right)\right) + \frac{T^2}{(4\pi)^2}\left[\frac{(2+3L_b)}{24}(3g_2^2 + g_1^2)\lambda_{hs} - L_b\left(\left(\lambda_1 + \frac{7}{12}\lambda_{hs} + \frac{1}{2}\lambda_s\right)\lambda_{hs} + \frac{9}{4}\lambda_s^2\right) - \frac{N_c}{12}(3L_b - L_f)y_t^2\lambda_{hs}\right].$$

The other parameters which are used in the above expressions are computed as follows:

$$
\begin{aligned}
g_{2,3}^2 &= g_2^2(\Lambda)T\left[1+\frac{g_2^2}{(4\pi)^2}\left(\frac{43}{6}L_b+\frac{2}{3}-\frac{(N_c+1)n_f}{3}L_f\right)\right],\\
g_{1,3}^2 &= g_1^2(\Lambda)T\left[1-\frac{g_1^2}{(4\pi)^2}\frac{1}{6}(L_bY_\phi^2+L_fY_{2f}n_f)\right],\\
h_3 &= \frac{g_2^2(\Lambda)T}{4}\left[1+\frac{1}{(4\pi)^2}\left(\left(\frac{43}{6}L_b+\frac{17}{2}-\frac{(N_c+1)n_f}{3}(L_f-1)\right)g_2^2+\frac{g_1^2}{2}-2N_cy_t^2+12\lambda_1\right)\right],\\
h_3' &= \frac{g_1^2(\Lambda)T}{4}\left[1+\frac{1}{(4\pi)^2}\left(\frac{3g_2^2}{2}-\frac{1}{6}((L_b-1)Y_\phi^2+(L_f-1)Y_{2f}n_f)g_1^2-2(Y_q^2+Y_u^2)N_cy_t^2+12\lambda_1\right)\right],\\
h_3'' &= \frac{g_2(\Lambda)g_1(\Lambda)T}{2}\left[1+\frac{1}{(4\pi)^2}\left(\left(\frac{43}{12}L_b-1\right)g_2^2-\frac{Y_\phi^2}{3}\left(\frac{1}{4}L_b-1\right)g_1^2+4\lambda_1+\frac{2}{3}N_cy_t^2-(L_f-1)\left(\frac{N_c+1}{6}g_2^2+\frac{Y_{2f}}{12}g_1^2\right)n_f\right)\right].
\end{aligned}
\tag{6.15}
$$

With the inclusion of two-loop corrections to the thermal masses especially to m_S and the Higgs, the upper bound on the singlet mass coming from the first-order phase transition and the current Higgs mass bound remains the same. Since the two-loop corrections are less for the chosen benchmark point from Planck-scale perturbativity, the strength of the order of the phase transition does not change significantly, and the Higgs mass bound is now satisfied in the 1σ limit with this slight change.

B. Triplet extension

In a similar way, the scalar potential given in Eq. (3.1) for the inert triplet in the DR3EFTs is given as

$$
V = -\mu_3^2H^\dagger H+m_{T,3}^2\mathrm{Tr}(T^\dagger T)+\lambda_{1,3}|H^\dagger H|^2+\lambda_{t,3}(\mathrm{Tr}|T^\dagger T|)^2+\lambda_{ht,3}H^\dagger H\mathrm{Tr}(T^\dagger T). \tag{6.16}
$$

The matching relations for the corresponding quartic couplings are given as

$$
\begin{aligned}
\lambda_{1,3} = T\Bigg[\lambda_1(\Lambda)+\frac{1}{(4\pi)^2}\Bigg[&\frac{1}{8}(3g_2^4+g_1^4+2g_2^2g_1^2)+3L_f(y_t^4-2\lambda_1y_t^2)\\
&-L_b\left(\frac{3}{16}(3g_2^4+g_1^4+2g_1^2g_2^2)-\frac{3}{2}(3g_2^2+g_1^2-8\lambda_1)\lambda_1+\frac{3}{4}\lambda_{ht}^2\right)\Bigg]\Bigg],
\end{aligned}
\tag{6.17}
$$

$$
\lambda_{ht,3} = T\left[\lambda_{ht}(\Lambda)+\frac{1}{(4\pi)^2}\left[2g_2^4-3\lambda_{ht}y_t^2L_f-L_b\left(2\lambda_{ht}^2+5\lambda_{ht}\lambda_t+3g_2^4+6\lambda_{ht}\lambda_1-\frac{3}{4}\lambda_{ht}(g_1^2+11g_2^2)\right)\right]\right], \tag{6.18}
$$

$$
\lambda_{t,3} = T\left[\lambda_t(\Lambda)+\frac{1}{(4\pi)^2}[4g_2^4-L_b(\lambda_{ht}^2+11\lambda_t^2-12g_2^2\lambda_t+6g_2^4)]\right], \tag{6.19}
$$

where

$$
L_b = \ln\left(\frac{\Lambda^2}{T^2}\right)-2[\ln(4\pi)-\gamma], \tag{6.20}
$$

$$
L_f = L_b+4\ln 2. \tag{6.21}
$$

The matching relations for the corresponding bare mass parameters are given as [110]

$$
\begin{aligned}
\mu_3^2 = (\mu_3^2)_{\mathrm{SM}}+\frac{T^2}{8}\lambda_{ht}(\Lambda)+\frac{1}{16\pi^2}\Bigg[&+\frac{3}{2}\lambda_{ht}m_T^2L_b+T^2\left(\frac{5}{24}g_2^4+\frac{1}{2}\lambda_{ht}g_2^2-\frac{3}{8}\lambda_{ht}y_t^2L_f+L_b\left(-\frac{7}{16}g_2^4-\frac{5}{8}\lambda_{ht}^2\right.\right.\\
&\left.\left.-\frac{5}{8}\lambda_{ht}\lambda_t+\frac{33}{32}\lambda_{ht}g_2^2+\frac{3}{32}\lambda_{ht}g_1^2-\frac{3}{4}\lambda_{ht}\lambda_1\right)+\left(c+\ln\left(\frac{3T}{\Lambda_{3d}}\right)\right)\left(-\frac{3}{2}\lambda_{ht,3}^2+6\lambda_{ht,3}g_{2,3}^2-\frac{3}{4}g_{2,3}^4\right)\right)\Bigg],
\end{aligned}
\tag{6.22}
$$

where

$$(\mu_3^2)_{\rm SM} = -\mu^2(\Lambda) + \frac{T^2}{16}(3g_2^2(\Lambda) + g_1^2(\Lambda) + 4y_t^2(\Lambda) + 8\lambda_1(\Lambda)) + \frac{1}{16\pi^2}\left[-\mu^2\left(\left(\frac{3}{4}(3g_2^2+g_1^2) - 6\lambda_1\right)L_b - 3y_t^2 L_f\right)\right.$$
$$+ T^2\left(\frac{167}{96}g_2^4 + \frac{1}{288}g_1^4 - \frac{3}{16}g_2^2g_1^2 + \frac{1}{4}\lambda_1(3g_2^2+g_1^2) + L_b\left(\frac{17}{16}g_2^4 - \frac{5}{48}g_1^4 - \frac{3}{16}g_2^2g_1^2 + \frac{3}{4}\lambda_1(3g_2^2+g_1^2) - 6\lambda_1^2\right)\right.$$
$$+ \left(c + \ln\left(\frac{3T}{\Lambda_{3d}}\right)\right)\left(\frac{39}{16}g_{2,3}^4 - \frac{5}{16}g_{1,3}^4 - \frac{9}{8}g_{2,3}^2g_{1,3}^2 + 12g_{2,3}^2h_3 - 6h_3^2 - 2h_3'^2 - 3h_3''^2 + 3\lambda_{1,3}(3g_{2,3}^2+g_{1,3}^2) - 12\lambda_{1,3}^2\right)$$
$$- y_t^2\left(\frac{3}{16}g_2^2 + \frac{11}{48}g_1^2 + 2g_s^2\right) + \left(\frac{1}{12}g_2^4 + \frac{5}{108}g_1^4\right)N_f + L_f\left(y_t^2\left(\frac{9}{16}g_2^2 + \frac{17}{48}g_1^2 + 2g_s^2 - 3\lambda_1\right) + \frac{3}{8}y_t^4\right.$$
$$\left.\left.\left. - \left(\frac{1}{4}g_2^4 + \frac{5}{36}g_1^4\right)N_f\right) + \ln(2)\left(y_t^2\left(-\frac{21}{8}g_2^2 - \frac{47}{72}g_1^2 + \frac{8}{3}g_s^2 + 9\lambda_1\right) - \frac{3}{2}y_t^4 + \left(\frac{3}{2}g_2^4 + \frac{5}{6}g_1^4\right)N_f\right)\right)\right] \tag{6.23}$$

and

$$m_{T,3}^2 = -m_T^2 + T^2\left(\frac{1}{6}\lambda_{ht}(\Lambda) + \frac{5}{12}\lambda_t(\Lambda) + \frac{1}{2}g_2^2(\Lambda)\right)\frac{1}{16\pi^2}\left[-(6g_2^2 - 5\lambda_t)m_T^2L_b + 2\mu^2\lambda_{ht}L_b + T^2\left(\left(\frac{71}{18} + \frac{2}{9}N_f\right)g_2^4\right.\right.$$
$$+ \frac{5}{3}\lambda_t g_2^2 + \frac{1}{4}\lambda_{ht}g_2^2 + \frac{1}{12}\lambda_{ht}g_1^2 + L_b\left(\frac{5}{12}g_2^4 - \frac{3}{4}\lambda_{ht}^2 - \frac{55}{12}\lambda_t^2 + \frac{11}{8}\lambda_{ht}g_2^2 + \frac{1}{8}\lambda_{ht}g_1^2 + 5\lambda_t g_2^2 - \frac{5}{6}\lambda_{ht}\lambda_t - \lambda_{ht}\lambda_1\right)$$
$$+ \left(c + \ln\left(\frac{3T}{\Lambda_{3d}}\right)\right)(-2\lambda_{ht,3}^2 - 10\lambda_{t,3}^2 + \lambda_{ht,3}(3g_{2,3}^2 + g_{1,3}^2) + 20\lambda_{t,3}g_{2,3}^2 - 3g_{2,3}^4 + 24g_{2,3}^2\delta_3 - 24\delta_3^2 + 8g_{2,3}^2\delta_3'$$
$$\left.\left. - 16\delta_3\delta_3' - 16\delta_3'^2) - L_f\left(\frac{1}{2}\lambda_{ht}y_t^2 + \frac{2}{3}g_2^4N_f\right) + \ln(2)(3\lambda_{ht}y_t^2 + 4g_2^4N_f)\right)\right]. \tag{6.24}$$

Below are the expressions for the quantities which are used above:

$$g_{2,3}^2 = g_2^2(\Lambda)T\left[1 + \frac{g_2^2}{(4\pi)^2}\left(\frac{44 - N_d - 2N_t}{6}L_b + \frac{2}{3} - \frac{4N_f}{3}L_f\right)\right], \tag{6.25}$$

$$g_{1,3}^2 = g_1^2(\Lambda)T\left[1 + \frac{g_1^2}{(4\pi^2)}\left(-\frac{N_d}{6}L_b - \frac{20N_f}{9}L_f\right)\right], \tag{6.26}$$

$$h_3 = \frac{g_2^2(\Lambda)T}{3}\left(1 + \frac{1}{(4\pi)^2}\left[\left(\frac{44 - N_d - 2N_t}{6}L_b + \frac{53}{6} - \frac{N_d}{3} - \frac{2N_t}{3} - \frac{4N_f}{3}(L_f - 1)\right)g_2^2 + \frac{g_1^2}{2} - 6y_t^2 + 12\lambda_1 + 8\lambda_{ht}\right]\right),$$
$$h_3' = \frac{g_1^2(\Lambda)T}{4}\left(1 + \frac{1}{(4\pi)^2}\left[\frac{3g_2^2}{2} + \left(\frac{1}{2} - \frac{N_d}{6}(2 + L_b) - \frac{20N_f}{9}(L_f - 1)\right)g_1^2 - \frac{34}{3}y_t^2 + 12\lambda_1\right]\right), \tag{6.27}$$

$$h_3'' = \frac{g_2(\Lambda)g_1(\Lambda)T}{2}\left(1 + \frac{1}{(4\pi)^2}\left[-\frac{5 + N_d}{6}g_2^2 + \frac{3 - N_d}{6}g_1^2 + L_b\left(\frac{44 - N_d}{12}g_2^2 - \frac{N_d}{12}g_1^2\right)\right.\right.$$
$$\left.\left. - N_f(L_f - 1)\left(\frac{2}{3}g_2^2 + \frac{10}{9}g_1^2\right) + 2y_t^2 + 4\lambda_1\right]\right), \tag{6.28}$$

$$\delta_3 = \frac{1}{2}g_2^2(\Lambda)T\left(1 + \frac{1}{(4\pi)^2}\left[\lambda_{ht} + 8\lambda_t + g_2^2\left(\frac{16 - N_d - 2N_t}{3} - \frac{4}{3}N_f(L_f - 1) + L_b\frac{44 - N_d - 2N_t}{6}\right)\right]\right), \tag{6.29}$$

$$\delta_3' = -\frac{1}{2}g_2^2(\Lambda)T\left(1 + \frac{1}{(4\pi)^2}\left[4\lambda_t + g_2^2\left(-\frac{20 + N_d + 2N_t}{3} - \frac{4}{3}N_f(L_f - 1) + L_b\frac{44 - N_d - 2N_t}{6}\right)\right]\right). \tag{6.30}$$

where $N_d = 1$, $N_t = 1$, and $N_f = 3$ to identify the contributions from the SM Higgs doublet, the real triplet, and the fermions, respectively.

In the case of the triplet, there is a significant change after the two-loop corrections to the thermal masses are added. The upper mass bound which was previously 310 GeV is now constrained more and reduced to 259 GeV.

C. Constraints from DM relic

Both complex singlet and inert triplet scenarios considered here offer a dark matter candidate being odd under Z_2. In order to fulfill the criteria of only dark matter candidate, the neutral component in both scenarios independently should satisfy the observed dark matter relic by the Planck experiments [111]:

$$\Omega_{\rm DM}h^2 = 0.1199 \pm 0.0027. \tag{6.31}$$

The interactions of the Z_2 odd particles with the particles in the thermal bath are the gauge couplings and the quartic couplings, and the values of these couplings are quite large. Hence, the DM particle is considered to be in equilibrium with the thermal bath initially. As the Universe expands, the interaction rates of the DM falls short to maintain the equilibrium number density and freezes out. After freeze-out, the number density of the DM remains constant in the comoving frame, which gives the DM relic abundance in the current epoch. So, we constrain our parameter space to satisfy the thermal relic abundance as given in Eq. (6.31). In the case of the singlet, the main annihilation comes via an s-channel Higgs boson on or off shell. It is noticed that for maximum region of parameter space the singlet dark matter can satisfy the required observed dark matter relic [75,112,113] and, thus, seems phenomenologically much more viable. Contrastingly, in the inert triplet scenario, the neutral part T^0 annihilates mainly W^+W^- and coannihilates via $T^\pm T^0 \to W^\pm Z$ and, thus, demands $m_{T^0} \geq 1176$ GeV [12] to satisfy the required dark matter relic in Eq. (6.31). This is incompatible with the demand of a first-order phase transition at $m_h = 125.5$ GeV that we just observed in the previous section which states $m_T < 193.00$ GeV and $m_{T^0} < 310.24$ GeV. For the first-order phase transition occurring at temperatures after the freeze-out of species, entropy injection during the first-order phase transition can lead to dilution of the relic species that has decoupled from the thermal bath in the early Universe. This dilution factor can reach only on the order of 10, in the case of purely bosonic models which still does not make the inert triplet model relic mass bound of TeV order viable [114]. Certainly, the inert triplet scenario cannot satisfy both demands: obtaining the first-order phase transition consistent with the current experimental Higgs boson mass bound and satisfying the dark matter relic. A simple gateway would be one more contributor, viz. singlet, in order to satisfy the dark matter relic, which would also enhance the possibility of the first-order phase transition even further [60–64].

VII. CALCULATING FREQUENCY DETECTABLE BY LISA, LIGO, AND BBO

The phase transition from symmetric phase to broken phase proceeds via bubble nucleation when bubbles of the false vacua nucleate in the sea of symmetric phase and then keep on expanding. These expanding bubbles collide and gives rise to GWs, which is described below. The frequencies of such gravitational waves can be estimated via thermal parameters which are described in the next subsections. Before we move on to the calculation of the frequencies of the gravitational waves, let us revisit the effective potential in order to implement in CosmoTransition [115]. The effective potential at finite temperature can be written as

$$V_{\rm eff} = V_{\rm tree} + V_1(\phi, 0) + V_1(\phi, T), \tag{7.1}$$

where $V_{\rm tree}$ is the tree-level potential, $V_1(\phi, 0)$ is the quantum correction at the zero temperature, and $V_1(\phi, T) = \Delta V_1(\phi, T) + \Delta V_{\rm daisy/ring}(\phi, T)$ as shown in Eq. (2.4). The one-loop quantum correction at zero temperature is estimated via the Coleman-Weinberg method [90] working in the Feynman gauge and also implemented in CosmoTransition [115]:

$$V_1(\phi, 0) = \pm \frac{1}{64\pi^2} \sum_i n_i m_i^4 \left[\log \frac{m_i^2}{Q^2} - c_i \right], \tag{7.2}$$

where n_i and m_i are the degrees of freedom and field-dependent masses as described in Eqs. (3.2), (3.3), and (3.6), respectively. Here, $+(-)$ signs come for bosonic (fermionic) degrees of freedom. The expression for the potential coming from nonzero temperature including the daisy/ring resummation (also in the Feynman gauge) are expressed as [115]

$$V_1(\phi, T) = \frac{T^2}{2\pi^2} \sum_i n_i J_\pm \left[\frac{m_i^2}{T^2} \right], \tag{7.3}$$

where $J_\pm$ are spline functions with $+(-)$ for bosons (fermions), respectively, and are defined as

$$J_\pm \left(\frac{m_i^2}{T^2} \right) = \pm \int_0^\infty dy y^2 \log \left(1 \mp e^{-\sqrt{y^2 + \frac{m_i^2}{T^2}}} \right). \tag{7.4}$$

Next, we discuss the relevant parameters needed to calculate the frequencies of the GWs using CosmoTransition [115] and BubbleProfiler [116].

A. Thermal parameters

GWs are created when bubble collision occurs and, thus, depend on the bubble nucleation rate as given below [65]:

$$\Gamma(t) = A(t)e^{-S_3(t)}, \tag{7.5}$$

where S_3 is the Euclidean action of the background field ϕ written in spherical polar coordinate of the critical bubble as follows [65]:

$$S_3 = 4\pi \int dr r^2 \left[\frac{1}{2}(\partial_r \vec{\phi})^2 + V_{\text{eff}}\right]. \tag{7.6}$$

Here, V_{eff} is the total potential as given in Eq. (7.1).

The temperature of the thermal bath at time t_* is defined as T_* and without significant reheating effect, $T_* \sim T_n$, the nucleation temperature. At the nucleation temperature T_n, the bubble nucleation starts, and the bubble nucleation rate Γ should be large enough that a bubble is nucleated per horizon volume with probability of the order of 1 [65]. In terms of bubble nucleation rate, the inverse time duration of the phase transition, β, is given as

$$\beta = -\left.\frac{dS}{dt}\right|_{t=t_*} \simeq \frac{\dot{\Gamma}}{\Gamma}, \tag{7.7}$$

t_* being the instant of time where the first-order phase transition completes. The parameter β defines the time variation of the bubble nucleation rate and, therefore, describes the length of the time in which the phase transition occurs. There are two relevant parameters which control the GW signal; one of them is the fraction $\frac{\beta}{H_*}$, where H_* is the Hubble parameter at temperature T_*. To achieve a large GW signal, a relatively slow phase transition is required, and, hence, the fraction $\frac{\beta}{H_*}$ should be small for stronger signals. The ratio $\frac{\beta}{H_*}$ instrumental for this is defined as

$$\frac{\beta}{H_*} = T_* \left.\frac{dS}{dt}\right|_{T_*}, \tag{7.8}$$

where T_* is the temperature at time t_*, i.e., $T_* = T|_{t_*}$, and it becomes $T_* \simeq T_n$ with negligible reheating effect. The ratio $\frac{\beta}{H_*}$ required for the visible signal in LISA is $\frac{\beta}{H_*} \lesssim 10^3$ [117]. This is a dimensionless quantity, and it mainly depends on the effective potential size at the nucleation temperature. The other essential parameter is α, defined as the ratio of the vacuum energy density which is released during the phase transition to that of the radiation bath, and it is defined as below:

$$\alpha = \frac{\rho_{\text{vac}}}{\rho^*_{\text{rad}}}, \tag{7.9}$$

where $\rho^*_{\text{rad}} = g_* \pi^2 T_*^4/30$ and g_* is the number of relativistic degrees of freedom at temperature T_* in plasma. Other relevant parameters for the appraisal of the GW frequencies are

$$\kappa_v = \frac{\rho_v}{\rho_{\text{vac}}}, \qquad \kappa_\phi = \frac{\rho_\phi}{\rho_{\text{vac}}}, \tag{7.10}$$

where κ_v is the fraction of vacuum energy that is converted into bulk motion of the fluid and κ_ϕ is the fraction of vacuum energy converted into gradient energy of the Higgs-like field. And v_w is defined as the fluid bubble wall velocity.

B. Production of the gravitational wave signal

The first-order phase transition happens via bubble nucleation, and, because of the pressure difference between the false and true vacua, these bubbles start expanding. The collision of these bubbles then breaks the spherical symmetry of each bubble, and GWs are produced, while for uncollided bubbles the spherical symmetry remains preserved and no GWs are produced. The gravitational wave background spectrum arising from cosmological phase transition depends on various sources. The sources which are most relevant for GWs depend on the dynamics of bubble expansion and the plasma as we discuss below.

C. Relevant contributions to the gravitational wave spectrum

The following processes are involved in first-order phase transition for the production of gravitational waves.

(i) *Bubble wall collision [118–123] and shocks in the plasma*.—The technique referred as "envelope approximation" is used in this scenario. In this approximation, the contribution of scalar field ϕ is considered in computing the GW spectrum.

(ii) *Sound waves in the plasma*.—When a part of energy released in the transition is dissipated as kinetic energy, resulting in the bulk motion of fluid in plasma [124–128].

(iii) *Bubble collision* leads to the formation of magnetohydrodynamic turbulence in the plasma [129–133].

These three processes generally coexist and linearly combine to give the contribution to the GW background as follows [134]:

$$h^2\Omega_{\text{GW}} \simeq h^2\Omega_\phi + h^2\Omega_{sw} + h^2\Omega_{\text{turb}}. \tag{7.11}$$

The detailed forms of each contribution are discussed successively.

1. Bubble collision

The scalar field contribution to the GW involved in the phase transition can be treated by envelope approximation [119,121]. In envelope approximation, the expanding bubbles are configured with the overlapping of the corresponding set of infinitely thin shells. Once the phase transition is completed, the envelope disappears and the production of GWs stops. It has been found that the peak frequency for the GW signal is determined by the average

size of the bubble at collision. The GW contribution to the spectrum using the envelope approximation via numerical simulations can be written as

$$h^2\Omega_{\rm env}(f) = 1.67\times10^{-5}\left(\frac{\beta}{H}\right)^{-2}\left(\frac{\kappa_\phi\alpha}{1+\alpha}\right)^2\left(\frac{100}{g_*}\right)^{1/3} \times\left(\frac{0.11v_w^3}{0.42+v_w^2}\right)\frac{3.8(f/f_{\rm env})^{2.8}}{1+2.8(f/f_{\rm env})^{3.8}}, \quad (7.12)$$

with

$$\beta = \left[HT\frac{d}{dT}\left(\frac{S_3}{T}\right)\right]\Big|_{T_n}, \quad (7.13)$$

where T_n is defined as the nucleation temperature and H_n is the Hubble parameter at temperature T_n. The estimation of the bubble wall velocity v_w used in the above equation is given as [122,135–137]

$$v_w = \frac{1/\sqrt{3}+\sqrt{\alpha^2+2\alpha/3}}{1+\alpha}. \quad (7.14)$$

The κ_ϕ parameter used in the calculation is defined as the fraction of latent heat deposited in a thin shell and is expressed as

$$\kappa_\phi = 1-\frac{\alpha_\infty}{\alpha}, \quad (7.15)$$

with [134,138]

$$\alpha_\infty = \frac{30}{24\pi^2 g_*}\left(\frac{v_n}{T_n}\right)^2\left[6\left(\frac{m_W}{v}\right)^2+3\left(\frac{m_Z}{v}\right)^2+6\left(\frac{m_t}{v}\right)^2\right], \quad (7.16)$$

where v and v_n are the vacuum expectation values of the Higgs field at the electroweak scale and at the nucleation temperature T_n, respectively. M_W, M_Z, and M_t are the W boson, Z boson, and top-quark masses, respectively. α is defined in Eq. (7.10) at the nucleation temperature, where

$$\rho_{\rm vac} = \left[\left(V_{\rm eff}^{\rm high}-T\frac{dV_{\rm eff}^{\rm high}}{dT}\right)-\left(V_{\rm eff}^{\rm low}-T\frac{dV_{\rm eff}^{\rm low}}{dT}\right)\right] \quad (7.17)$$

and

$$\rho_{\rm rad}^* = \frac{g_*\pi^2T_n^4}{30}. \quad (7.18)$$

Finally, we receive the expression of the peak frequency $f_{\rm env}$, produced by bubble collisions, which contribute to the GW spectrum as

$$f_{\rm env} = 16.5\times10^{-6}\ {\rm Hz}\left(\frac{0.62}{v_w^2-0.1v_w+1.8}\right)\left(\frac{\beta}{H}\right) \times\left(\frac{T_n}{100\ {\rm GeV}}\right)\left(\frac{g_*}{100}\right)^{\frac{1}{6}}. \quad (7.19)$$

2. Sound wave

The latent heat is released at the phase boundary during bubble expansion. This released energy in transition grows with the volume of the bubble as $\sim R^3$, and the energy that is transferred to the scalar bubble wall grows with the surface of bubble $\sim R^2$, where R is the radius of the bubble. This energy which is released into the fluid mostly contributes in reheating the plasma. A small fraction of this energy goes into the bulk motion of fluid which can give rise to GWs. Therefore, the contribution to the gravitational wave from the sound wave (SW) can be estimated as follows:

$$h^2\Omega_{\rm SW} = 2.65\times10^{-6}\left(\frac{\beta}{H}\right)^{-1}v_w\left(\frac{\kappa_v\alpha}{1+\alpha}\right)^2\left(\frac{g_*}{100}\right)^{-\frac{1}{3}} \times\left(\frac{f}{f_{\rm SW}}\right)^3\left[\frac{7}{4+3(\frac{f}{f_{\rm SW}})^2}\right]^2, \quad (7.20)$$

where the parameter κ_v, earlier defined in Eq. (7.10) as the fraction of latent heat which is transferred to the bulk motion of the fluid, can be rewritten as

$$\kappa_v = \frac{\alpha_\infty}{\alpha}\left[\frac{\alpha_\infty}{0.73+0.083\sqrt{\alpha_\infty}+\alpha_\infty}\right]. \quad (7.21)$$

The peak frequency contribution $f_{\rm SW}$ to the GW spectrum produced by sound wave mechanisms is

$$f_{\rm SW} = 1.9\times10^{-5}\ {\rm Hz}\left(\frac{1}{v_w}\right)\left(\frac{\beta}{H}\right)\left(\frac{T_n}{100\ {\rm GeV}}\right)\left(\frac{g_*}{100}\right)^{\frac{1}{6}}. \quad (7.22)$$

3. Turbulence

The collision of bubbles can also induce turbulent motion of fluid [139]. This can give rise to GWs even after the transition is finished. Lastly, the contribution to GWs from magnetohydrodynamic turbulence can be evaluated as

$$h^2\Omega_{\rm turb} = 3.35\times10^{-4}\left(\frac{\beta}{H}\right)^{-1}v_w\left(\frac{\epsilon\kappa_v\alpha}{1+\alpha}\right)^{\frac{3}{2}}\left(\frac{g_*}{100}\right)^{-\frac{1}{3}} \times\frac{\left(\frac{f}{f_{\rm turb}}\right)^3\left(1+\frac{f}{f_{\rm turb}}\right)^{-\frac{11}{3}}}{(1+\frac{8\pi f}{h_*})}, \quad (7.23)$$

where $\epsilon = 0.1$ and $f_{\rm turb}$ is again the peak frequency contribution to the GW spectrum produced by the turbulence mechanism

$$f_{\text{turb}} = 2.7 \times 10^{-5}\ \text{Hz}\left(\frac{1}{v_w}\right)\left(\frac{\beta}{H}\right)\left(\frac{T_n}{100\ \text{GeV}}\right)\left(\frac{g_*}{100}\right)^{\frac{1}{6}}, \tag{7.24}$$

where

$$h_* = 16.5 \times 10^{-6}\ \text{Hz}\left(\frac{T_n}{100\ \text{GeV}}\right)\left(\frac{g_*}{100}\right)^{\frac{1}{6}}. \tag{7.25}$$

The updated expression for κ_v given in Eq. (7.21) which is used in this analysis is as follows [140,141]:

$$\kappa_v \simeq \left[\frac{\alpha_\infty}{0.73 + 0.083\sqrt{\alpha_\infty} + \alpha_\infty}\right]. \tag{7.26}$$

D. Benchmark points

In this section, we compare the triplet and the singlet scenarios with their gravitational wave frequencies detectable by LISA, LIGO, and BBO experiments [85–87]. For this purpose, we choose the benchmark points (BPs) in the singlet and the triplet cases as given in Table III.

The thermal parameters required for the calculation of the GW spectrum are mainly the nucleation temperature T_n, the strength of phase transition α, length of the time of phase transition β, Higgs VEV at the nucleation temperature v_n, and the bubble wall velocity v_w. The calculation of the GW intensity requires the phase transition temperature. Hence, the finite temperature effective potential is computed for the calculation of the transition temperature. These calculations are performed using the publicly available package CosmoTransition [115]. The tree-level potential is given as an input to this package, and it provides the thermal parameters required for the calculation of GW intensity. These thermal parameters corresponding to the benchmark points in Table III, predicting a strongly first-order phase transition, and allowed by 125.5 GeV Higgs boson are shown in Tables IV and V for the singlet and the triplet scenarios, respectively.

The GW spectrum arising from the first-order phase transition for the benchmark points is given in Fig. 10. The constraints for different experiments are drawn by the respective sensitivity curves for the different GW detectors, viz. LISA, LIGO, and BBO. The higher value of α and lower value of β actually provide stronger GW signals. It is clear from Tables IV and V that the nucleation temperature T_n is lower than the critical temperature T_c for all benchmark points in singlet and triplet, and the value of ratio v_n/T_n is $\gtrsim 1$, giving a strongly first-order phase transition. The values of the nucleation temperature for inert triplet $T_n = 115.07(113.55)$ GeV are lower compared to singlet ones $T_n = 121.03(119.25)$ GeV that ensure stronger signals detectable by various experiments. For both the benchmark points, the GW intensity lies within the sensitivity curves of LISA and BBO in the singlet and the triplet scenarios, respectively. The detectable frequencies for a singlet lie between $\sim 1.15 \times 10^{-3}$ and 1.06×10^{-2} Hz, while for the triplet the allowed ranges enhance to range $\sim 4.18 \times 10^{-4}$–1.99×10^{-2} Hz for the LISA experiment as can be seen from Fig. 10. It is also inferred from Fig. 10 that the GW intensity mainly depends on the parameter β. The smallest value of parameter β is attained for BP2 of the inert triplet scenario, which leads to highest GW intensity. For LIGO, the GW intensities lie outside the detectable region in both the singlet and the triplet scenarios. In comparison, BBO has more region of parameter space that can be detected for both, with the triplet having a larger spectrum with a slightly larger frequency range compared to the singlet case. Also, the SNR for a particular detector is given as

$$\text{SNR} = \sqrt{2t_{\text{obs}}\int_{f_{\text{min}}}^{f_{\text{max}}} df\left[\frac{\Omega_{\text{GW}}(f)h^2}{\Omega_{\text{noise}}(f)h^2}\right]^2},$$

where t_{obs} is defined as the duration of the observation in unit of seconds and $\Omega_{\text{noise}}(f)h^2$ is defined as the effective strain noise power spectral density for the considered

TABLE III. BPs for frequency analysis for singlet and triplet scenarios.

	m_S/m_T	λ_s/λ_t	$\lambda_{hs}/\lambda_{ht}$
BP1	150.23	0.10	0.10
BP2	120.23	0.01	0.01

TABLE IV. Thermal parameters required for frequency analysis of the singlet for the chosen benchmark points, where T_n is the nucleation temperature, α is the strength of transition, β is the length of the time of phase transition, and v_n is the Higgs VEV at the nucleation temperature.

	BP1	BP2
T_n [GeV]	121.03	119.25
α	0.17	0.18
β/H	332.83	327.94
v_n/T_n	1.10	1.16

TABLE V. Thermal parameters required for frequency analysis of the inert triplet for the chosen benchmark points, where T_n is the nucleation temperature, α is the strength of transition, β is the length of the time of phase transition, and v_n is the Higgs VEV at the nucleation temperature.

	BP1	BP2
T_n [GeV]	115.07	113.55
α	0.86	0.89
β/H	284.22	278.87
v_n/T_n	1.16	1.22

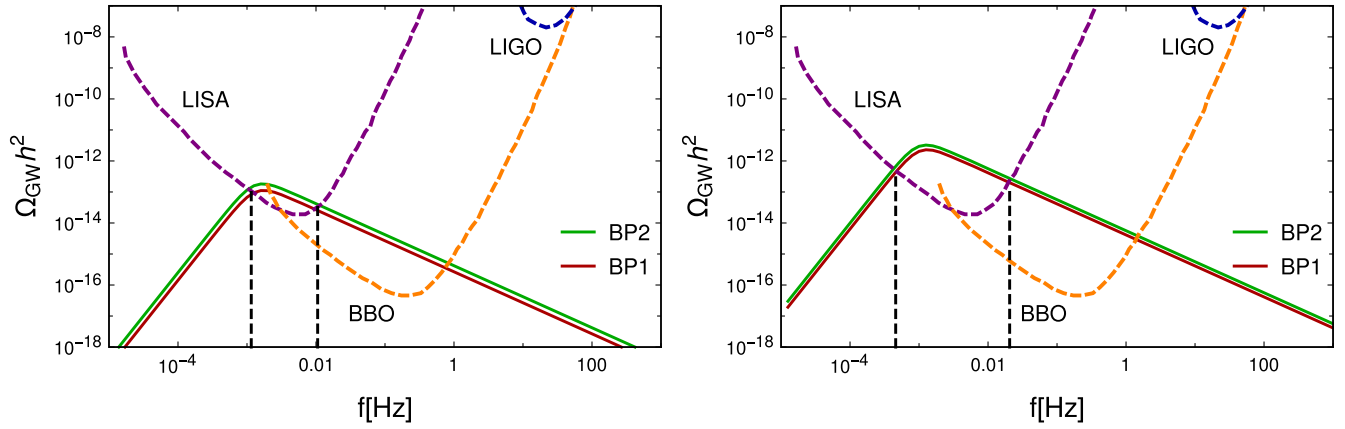

(a) Singlet (b) Triplet

FIG. 10. GW spectrum for the BPs allowed by a strongly first-order phase transition in comparison with the sensitivity curves based on noise curves of experiments, i.e., LISA, LIGO, and BBO. The value of nucleation temperature (T_n), the strength of transition (α), and the length of the time of phase transition (β) are computed and used for the GW intensity calculation.

detector. $\Omega_{\rm GW}(f)$ is detectable for SNR > 1, which is possible for $\Omega_{\rm noise}(f) < \Omega_{\rm GW}$. Therefore, there is a finite chance that the frequency range in Fig. 10 covered by the BBO experiment is detectable [142–147].

However, future advanced GW detectors such as eLISA and BBO are expected to explore millihertz to decihertz of frequency ranges in the future. Similarly, ground-based detectors like aLIGO can explore the lower frequency range with much higher sensitivity. There can be 2–3 orders-of-magnitude theoretical uncertainty in the peak GW amplitude using the daisy-resummation approach due to renormalization scale dependence. Using higher-order terms in the perturbative calculations, i.e., the dimensional reduction approach, the scale dependence can be reduced and the theoretical uncertainty can be reduced to $\mathcal{O}(10^0$–$10^1)$ [107,148].

In order to ensure that the physical quantities in any field theory are independent of the particular renormalization scheme (RS), if the true result is exactly RS independent, then the best approximation should be least sensitive to the small changes in the RS. This is known as the principle of minimal sensitivity [149]. This principle states that, for unphysical parameters, the exact result is a constant. Hence, the calculated result cannot be a successful approximation where it is varying rapidly. If the variation is considered with the renormalization scale, then the extrapolation from 10^2 GeV can be judged by observing how flat the result is at higher scales. The variation will not be flat everywhere, so one can always choose the scale to lie in the middle of the flat portion of the variation. The variation of all the quartic couplings becomes almost constant after 10^6 GeV and further higher scales. Therefore, we consider the variation of the quartic couplings using the two-loop β functions in the daisy-resummation approach including the two-loop potential from Eqs. (5.6) and (5.7) at three different scales, i.e., 10^2, 10^3, and 10^6 GeV, respectively. The benchmark points and the thermal parameters for singlet and triplet scenarios are given in Tables VI–VIII.

The GW spectrum for the singlet and the triplet scenarios is given in Fig. 11. The blue and the green intensity curves correspond to the singlet and the triplet scenarios, respectively, and the dotted purple, orange, and cyan curves denote the intensity spectrum for LISA, BBO, and LIGO experiments, respectively. The gravitational wave spectrum

TABLE VI. Allowed benchmark points for the frequency analysis in singlet and triplet scenarios at three different renormalization scales, i.e., 10^2, 10^3, and 10^6 GeV using the daisy-resummation method with two-loop potential and two-loop β functions. The quartic couplings are given for three different renormalization scale variations followed by the running of the two-loop β functions.

μ (GeV)	m_S/m_T (GeV)	λ_s/λ_t	$\lambda_{hs}/\lambda_{ht}$	λ_h
10^2	190.23	0.10	0.33	0.1264
10^3	190.23	0.11/0.11	0.36/0.36	0.1040/0.1040
10^6	190.23	0.19/0.22	0.48/0.53	0.1198/0.1253

TABLE VII. Thermal parameters required for the frequency analysis in the case of a singlet for chosen benchmark points, where T_n is the nucleation temperature, α is the strength of transition, β is the length of the time of phase transition, and v_n is the Higgs VEV at the nucleation temperature.

	10^2	10^3	10^6
T_n [GeV]	130.73	131.69	185.91
α	0.15	0.15	0.10
β/H	292.83	295.94	327.68
v_n/T_n	0.97	0.97	0.83

TABLE VIII. Thermal parameters required for the frequency analysis in the case of the inert triplet for chosen benchmark points, where T_n is the nucleation temperature, α is the strength of transition, β is the length of the time of phase transition, and v_n is the Higgs VEV at the nucleation temperature.

	10^2	10^3	10^6
T_n [GeV]	128.50	129.60	181.07
α	0.16	0.16	0.11
β/H	291.56	294.23	320.68
v_n/T_n	0.98	0.98	0.84

is then considered for three different renormalization scales (μ), i.e., 10^2, 10^3, and 10^6 GeV in Figs. 11(a), 11(b), and 11(c), respectively. The nucleation temperature for the triplet is lower than the singlet scenarios for the three renormalization scales as can be read from Tables VII and VIII. It can be noted that the nucleation temperature increases with the renormalization scale and, nevertheless, remains lower for the triplet compared to the singlet. The increase in the nucleation temperature with the renormalization scale actually reduces the GW intensity and, thus, the detectable frequency range by LISA, LIGO, and BBO experiments for both singlet and triplet scenarios. Using Tables VII and VIII, the uncertainty in the computation of the gravitational wave intensity due to the renormalization scale dependency is given in Fig. 12 for both the singlet and the triplet scenarios. The uncertainty band depicts the variation of the results with the renormalization scale using the daisy-resummation method including the two-loop potential and two-loop β functions. It can be seen from Fig. 11 that the changes in the gravitational wave intensity from 10^2 to 10^3 GeV scale are minuscule. Hence, in order to show a significant amount of scale dependency, we choose 10^2 and 10^6 GeV scales, respectively, in Tables VII and VIII.

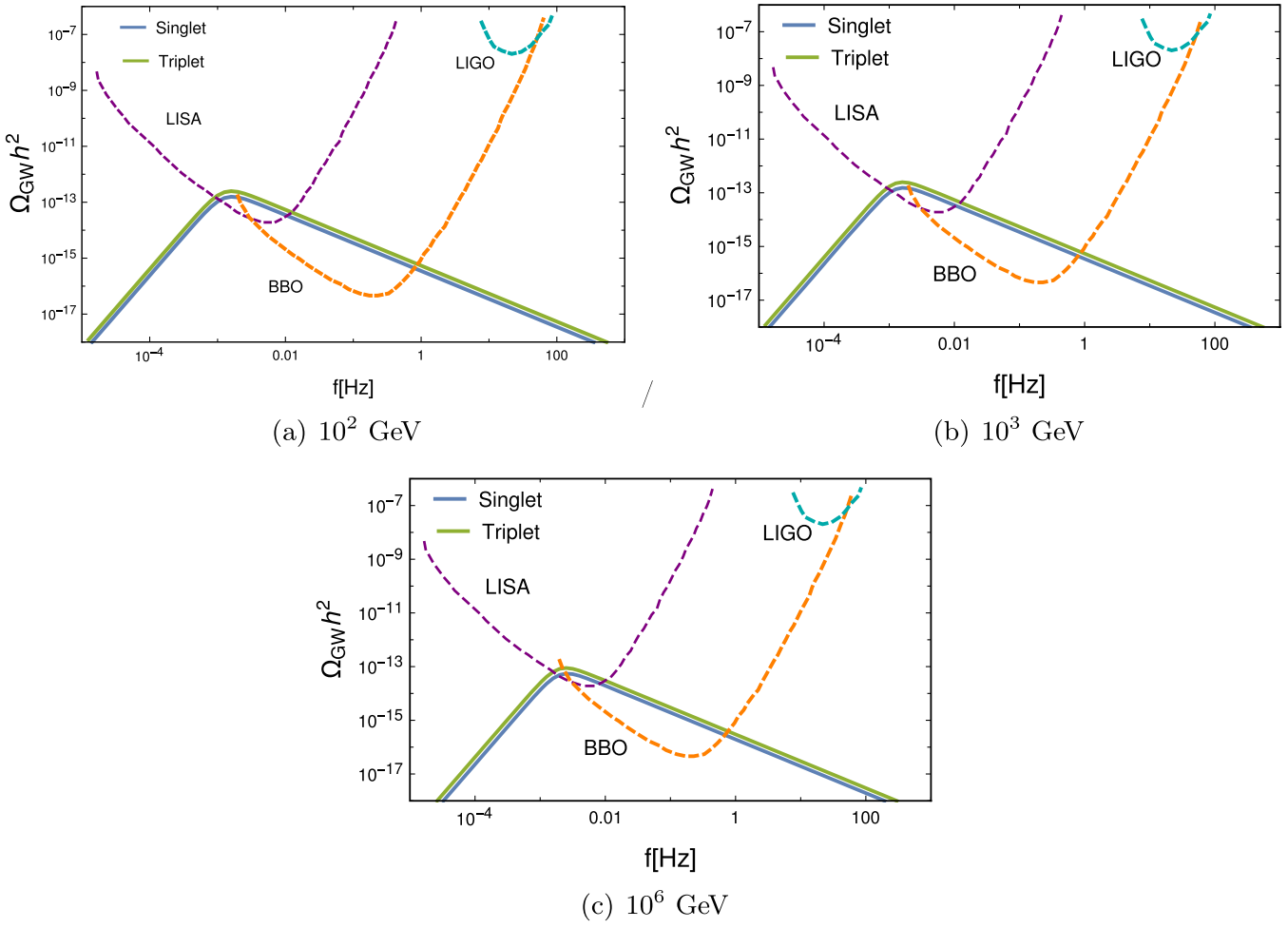

(a) 10^2 GeV

(b) 10^3 GeV

(c) 10^6 GeV

FIG. 11. GW spectrum for the BP allowed by a strongly first-order phase transition and perturbative unitarity in comparison with the sensitivity curves based on noise curves of experiments, i.e., LISA, LIGO, and BBO for three different renormalization scales, i.e., 10^2, 10^3, and 10^6 GeV using the daisy-resummation method including the two-loop potential and two-loop β functions. The blue and green curves correspond to the singlet and the triplet scenarios, respectively. The dotted purple, orange, and cyan curves denote the sensitivity curves from LISA, BBO, and LIGO experiments, respectively.

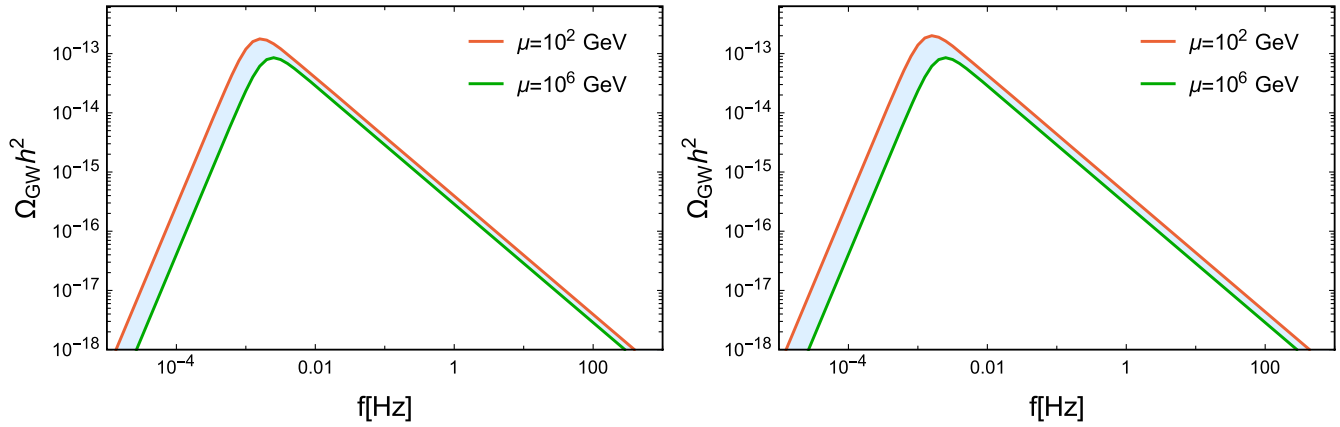

(a) Singlet (b) Triplet

FIG. 12. Uncertainty band for the scale dependence of the gravitational wave intensity in both singlet and the triplet using the daisy-resummation method including the two-loop potential and two-loop β functions. The uncertainty band depicts the variation as a result of the change in the renormalization scale. The red and the green colors correspond to the gravitational wave intensity for 10^2 and 10^6 GeV renormalization scale, respectively.

In this article, we showed how the parameters satisfying the first-order phase transition and the gravitational wave signatures are different for both scenarios. The effect of two-loop corrections to the potentials are considered, in which only the triplet mass bound gets affected slightly. Another interesting fact is that the upper mass bound for singlet is larger, i.e., $\sim$1 TeV, compared to the triplet $\lesssim$320 GeV. The nucleation temperature is lower for the triplet in comparison to the singlet, and the detectable frequency range by LISA is more for the triplet, i.e., $\sim 4.18 \times 10^{-4}$ –1.99×10^{-2} Hz, in comparison to the singlet, i.e., $\sim 1.15 \times 10^{-3}$–1.06×10^{-2} Hz.

There are other aspects of the collider and dark matter phenomenology in which the scenarios can be easily discerned. The singlet does not have a charged Higgs boson like the triplet one, which can give rise to a displaced pion at the collider due to the compressed spectrum [12,74,75,83]. $Y = 0$ triplet unlike the SM doublet does not couple to fermions which alters the bounds on rare B decays [76,79] and also difficult to produce at the collider. However, vector boson fusion to charged Higgs and other associate production can be analyzed in the ZW decay mode of the charged Higgs via multilepton final states, where the triplet takes a VEV [80–82]. On the contrary, the singlet does not have any charged Higgs bosons, and, being gauge singlet, it cannot be produced via gauge bosons. The productions mainly come via the mixing with the SM Higgs bosons or SM Higgs boson decay to a singlet pair [35,118], and for an inert singlet it is bounded by Higgs to invisible decay width [40,119]. Lastly, the inert singlet model satisfies the DM relic density bound even with the very small singlet mass along with the first-order phase transition [115–117], but for the triplet it shows underabundance, demanding such low triplet mass required for the first-order phase transition [75].

VIII. CONCLUSION

In this article, we study the $Y = 0$ $SU(2)$ inert triplet which successfully stabilizes the electroweak vacuum at zero temperature and also provide the DM candidate [12] at finite temperature. The regions of parameter space suitable for the first-order phase transitions are designated considering perturbative unitarity at one- and two-loop level along with the demand of a SM-like Higgs boson around 125.5 GeV. It has been noticed that no consistent solutions have been found at one-loop perturbativity till Planck scale consistent with a first-order phase transition and current Higgs boson and top-quark masses. Considering the two-loop beta functions with the one-loop resummed potential, one can find the maximum mass values for the singlet and the triplet field as 909 and 310 GeV, respectively, predicting the first-order phase transition, which are also consistent with the currently measured Higgs boson and top-quark masses. Including the two-loop contributions coming from the effective potential as well as the thermal masses, the mass bound for the singlet remains the same while satisfying the current Higgs mass within the uncertainty of 1σ. On the other hand, the mass bound for the inert triplet is further constrained to $\lesssim$259 GeV with these corrections. However, these maximum allowed values of mass correspond to relatively larger values of $\lambda_{hs}(\lambda_{ht}) = 4.00(1.95)$, respectively. For lower values of these masses correspond to the regions with higher $\frac{\phi_+(T_c)}{T_c}$, i.e., a more strongly first-order phase transition. The self-couplings of the singlet and the triplet are considered to be zero to maximize the $\frac{\phi_+(T_c)}{T_c}$.

It is interesting to note here that for the singlet mass $\lesssim$ 909 GeV one not only realizes a first-order phase transition along with a Higgs boson mass around 125.5 GeV, but also finds the parameter space consistent with a DM relic [75,112,113]. On the contrary, the situation looks grim for the triplet scenario, as the correct DM relic

abundance demands the triplet scalar mass $\lesssim$1.2–1.8 TeV. Thus, with only triplet extension of the SM, we cannot have the first-order phase transition along with the correct DM relic. Triplet DM mass < 320 GeV gives rise to underabundance for the DM, and we need additional fields to satisfy the correct relic [75].

A first-order phase transition in both cases can give rise to a gravitational wave coming from the bubble collision, sound wave of the plasma, and the turbulence. These add up to the frequencies that can be observed via the space- and Earth-based experiments like LISA [86], BBO [85], and LIGO [87]. To observe and distinguish the singlet and the triplet scenarios, we benchmark both singlet and triplet scenarios and predict their frequencies observed by various different detectors. The detectable frequency range by LISA is more for the triplet, i.e., $\sim 4.18 \times 10^{-4}$ – 1.99×10^{-2} Hz, in comparison to the singlet, i.e., $\sim 1.15 \times 10^{-3}$–1.06×10^{-2} Hz. For all the benchmark points, the GW intensities lie within the detectable range of LISA and BBO in both singlet and triplet scenarios. With the increase of the renormalization scale using the daisy-resummation method with two-loop β functions and two-loop potential, the GW intensity and also the detectable frequency drop. Thus, the singlet model, constrained from perturbative unitarity and DM relic, is in agreement with the sensitivity curves of GW detectors. However, for the triplet case, the strongly first-order phase transition predicts a relatively lower mass for the triplet ($\lesssim$320 GeV), demanding additional multiplets to satisfy the DM relic.

ACKNOWLEDGMENTS

P. B. thanks Science and Engineering Research Board (SERB) project (CRG/2018/004971) and MATRICS Grant No. MTR/2020/000668 for the financial support toward this work. P. B. also thanks Rajesh Gupta and Luigi Delle Rose for clearing some doubts. S. J. thanks Department of Science and Technology, Ministry of Science and Technology, India (DST)/INSPIRES/03/2018/001207 for the financial support toward finishing this work. This research was also supported by an appointment to the Young Scientist Training (YST) Program at the Asia Pacific Center for Theoretical Physics (APCTP) through the Science and Technology Promotion Fund and Lottery Fund of the Korean Government. This was also supported by the Korean Local Governments—Gyeongsangbuk-do Province and Pohang City. S. J. thanks Mariano Quiros, Nikita Blinov, Michael Bardsley, Csaba Balazs, and Anirban Karan for useful discussions.

APPENDIX A: TWO-LOOP β FUNCTIONS FOR ITM

1. Scalar quartic couplings

$$
\begin{aligned}
\beta_{\lambda=\lambda_1} = \frac{1}{16\pi^2}\Bigg[&\frac{27}{200}g_1^4 + \frac{9}{20}g_1^2 g_2^2 + \frac{9}{8}g_2^4 - \frac{9}{5}g_1^2\lambda_1 - 9g_2^2\lambda_1 + 24\lambda_1^2 + 8\lambda_{ht}^2 + 12\lambda_1 \mathrm{Tr}(Y_d Y_d^\dagger) + 4\lambda_1 \mathrm{Tr}(Y_e Y_e^\dagger) \\
&+ 12\lambda_1 \mathrm{Tr}(Y_u Y_u^\dagger) - 6\mathrm{Tr}(Y_d Y_d^\dagger Y_d Y_d^\dagger) - 2\mathrm{Tr}(Y_e Y_e^\dagger Y_e Y_e^\dagger) - 6\mathrm{Tr}(Y_u Y_u^\dagger Y_u Y_u^\dagger)\Bigg] + \frac{1}{(16\pi^2)^2} \\
&\times \Bigg[-\frac{3411}{2000}g_1^6 - \frac{1677}{400}g_1^4 g_2^2 - \frac{317}{80}g_1^2 g_2^4 + \frac{277}{16}g_2^6 + \frac{1887}{200}g_1^4\lambda_1 + \frac{117}{20}g_1^2 g_2^2\lambda_1 - \frac{29}{8}g_2^4\lambda_1 \\
&+ \frac{108}{5}g_1^2\lambda_1^2 + 108 g_2^2\lambda_1^2 - 312\lambda_1^3 + 10 g_2^4\lambda_{ht} + 32 g_2^2\lambda_{ht}^2 - 80\lambda_1\lambda_{ht}^2 - 128\lambda_{ht}^3 \\
&+ \frac{1}{20}(-5(64\lambda_1(-5g_3^2 + 9\lambda_1) - 90 g_2^2\lambda_1 + 9 g_2^4) + 9 g_1^4 + g_1^2(50\lambda_1 + 54 g_2^2))\mathrm{Tr}(Y_d Y_d^\dagger) \\
&- \frac{3}{20}(15 g_1^4 - 2 g_1^2(11 g_2^2 + 25\lambda_1) + 5(-10 g_2^2\lambda_1 + 64\lambda_1^2 + g_2^4))\mathrm{Tr}(Y_e Y_e^\dagger) - \frac{171}{100}g_1^4 \mathrm{Tr}(Y_u Y_u^\dagger) \\
&+ \frac{63}{10}g_1^2 g_2^2 \mathrm{Tr}(Y_u Y_u^\dagger) - \frac{9}{4}g_2^4 \mathrm{Tr}(Y_u Y_u^\dagger) + \frac{17}{2}g_1^2\lambda_1 \mathrm{Tr}(Y_u Y_u^\dagger) + \frac{45}{2}g_2^2\lambda_1 \mathrm{Tr}(Y_u Y_u^\dagger) + 80 g_3^2\lambda_1 \mathrm{Tr}(Y_u Y_u^\dagger) \\
&- 144\lambda_1^2 \mathrm{Tr}(Y_u Y_u^\dagger) + \frac{4}{5}g_1^2 \mathrm{Tr}(Y_d Y_d^\dagger Y_d Y_d^\dagger) - 32 g_3^2 \mathrm{Tr}(Y_d Y_d^\dagger Y_d Y_d^\dagger) - 3\lambda_1 \mathrm{Tr}(Y_d Y_d^\dagger Y_d Y_d^\dagger) \\
&- 42\lambda_1 \mathrm{Tr}(Y_d Y_u^\dagger Y_u Y_d^\dagger) - \frac{12}{5}g_1^2 \mathrm{Tr}(Y_e Y_e^\dagger Y_e Y_e^\dagger) - \lambda_1 \mathrm{Tr}(Y_e Y_e^\dagger Y_e Y_e^\dagger) - \frac{8}{5}g_1^2 \mathrm{Tr}(Y_u Y_u^\dagger Y_u Y_u^\dagger) \\
&- 32 g_3^2 \mathrm{Tr}(Y_u Y_u^\dagger Y_u Y_u^\dagger) - 3\lambda_1 \mathrm{Tr}(Y_u Y_u^\dagger Y_u Y_u^\dagger) + 30\mathrm{Tr}(Y_d Y_d^\dagger Y_d Y_d^\dagger Y_d Y_d^\dagger) - 12\mathrm{Tr}(Y_d Y_d^\dagger Y_d Y_u^\dagger Y_u Y_d^\dagger) \\
&+ 6\mathrm{Tr}(Y_d Y_u^\dagger Y_u Y_d^\dagger Y_d Y_d^\dagger) - 6\mathrm{Tr}(Y_d Y_u^\dagger Y_u Y_u^\dagger Y_u Y_d^\dagger) + 10\mathrm{Tr}(Y_e Y_e^\dagger Y_e Y_e^\dagger Y_e Y_e^\dagger) + 30\mathrm{Tr}(Y_u Y_u^\dagger Y_u Y_u^\dagger Y_u Y_u^\dagger)\Bigg],
\end{aligned}
$$

$$\beta_{\lambda_t} = \frac{1}{16\pi^2}\left[-24g_2^2\lambda_t + 88\lambda_t^2 + 8\lambda_{ht}^2 + \frac{3}{2}g_2^4\right] + \frac{1}{(16\pi^2)^2}\left[-\frac{68}{3}g_2^6 + 10g_2^4\lambda_{ht} + \frac{48}{5}g_1^2\lambda_{ht}^2 + 48g_2^2\lambda_{ht}^2 - 128\lambda_{ht}^3 + \frac{94}{3}g_2^4\lambda_t - 320\lambda_{ht}^2\lambda_t + 640g_2^2\lambda_t^2 - 4416\lambda_t^3 - 48\lambda_{ht}^2\mathrm{Tr}(Y_dY_d^\dagger) - 16\lambda_{ht}^2\mathrm{Tr}(Y_eY_e^\dagger) - 48\lambda_{ht}^2\mathrm{Tr}(Y_uY_u^\dagger)\right],$$

$$\beta_{\lambda_{ht}} = \frac{1}{16\pi^2}\left[\frac{3}{4}g_2^4 - \frac{9}{10}g_1^2\lambda_{ht} - \frac{33}{2}g_2^2\lambda_{ht} + 12\lambda_1\lambda_{ht} + 16\lambda_{ht}^2 + 24\lambda_{ht}\lambda_t + 6\lambda_{ht}\mathrm{Tr}(Y_dY_d^\dagger) + 2\lambda_{ht}\mathrm{Tr}(Y_eY_e^\dagger) + 6\lambda_{ht}\mathrm{Tr}(Y_uY_u^\dagger)\right] + \frac{1}{(16\pi^2)^2}\left[-\frac{9}{16}g_1^2g_2^4 + \frac{329}{48}g_2^6 + \frac{15}{2}g_2^4\lambda_1 + \frac{1671}{400}g_1^4\lambda_{ht} + \frac{9}{8}g_1^2g_2^2\lambda_{ht} - \frac{1087}{48}g_2^4\lambda_{ht} + \frac{72}{5}g_1^2\lambda_1\lambda_{ht} + 72g_2^2\lambda_1\lambda_{ht} - 60\lambda_1^2\lambda_{ht} + \frac{12}{5}g_1^2\lambda_{ht}^2 + 44g_2^2\lambda_{ht}^2 - 288\lambda_1\lambda_{ht}^2 - 168\lambda_{ht}^3 + 20g_2^4\lambda_t + 144g_2^2\lambda_{ht}\lambda_t - 576\lambda_{ht}^2\lambda_t - 544\lambda_{ht}\lambda_t^2 - \frac{1}{4}(3g_2^4 - 45g_2^2\lambda_{ht} + \lambda_{ht}(-160g_3^2 + 192\lambda_{ht} + 288\lambda - 5g_1^2))\mathrm{Tr}(Y_dY_d^\dagger) - \frac{1}{4}(-15g_2^2\lambda_{ht} + \lambda_{ht}(-15g_1^2 + 64\lambda_{ht} + 96\lambda_1) + g_2^4)\mathrm{Tr}(Y_eY_e^\dagger) - \frac{3}{4}g_2^4\mathrm{Tr}(Y_uY_u^\dagger) + \frac{17}{4}g_1^2\lambda_{ht}\mathrm{Tr}(Y_uY_u^\dagger) + \frac{45}{4}g_2^2\lambda_{ht}\mathrm{Tr}(Y_uY_u^\dagger) + 40g_3^2\lambda_{ht}\mathrm{Tr}(Y_uY_u^\dagger) - 72\lambda_1\lambda_{ht}\mathrm{Tr}(Y_uY_u^\dagger) - 48\lambda_{ht}^2\mathrm{Tr}(Y_uY_u^\dagger) - \frac{27}{2}\lambda_{ht}\mathrm{Tr}(Y_dY_d^\dagger Y_dY_d^\dagger) - 21\lambda_{ht}\mathrm{Tr}(Y_dY_u^\dagger Y_uY_d^\dagger) - \frac{9}{2}\lambda_{ht}\mathrm{Tr}(Y_eY_e^\dagger Y_eY_e^\dagger) - \frac{27}{2}\lambda_{ht}\mathrm{Tr}(Y_uY_u^\dagger Y_uY_u^\dagger)\right].$$

APPENDIX B: TWO-LOOP β FUNCTIONS FOR SINGLET

1. Scalar quartic couplings

$$\beta_\lambda^{(1)} = \frac{1}{16\pi^2}\left[\frac{27}{200}g_1^4 + \frac{9}{20}g_1^2g_2^2 + \frac{9}{8}g_2^4 - \frac{9}{5}g_1^2\lambda_1 - 9g_2^2\lambda_1 + 24\lambda_1^2 + 4\lambda_{hs}^2 + 12\lambda_1\mathrm{Tr}(Y_dY_d^\dagger) + 4\lambda_1\mathrm{Tr}(Y_eY_e^\dagger) + 12\lambda_1\mathrm{Tr}(Y_uY_u^\dagger) - 6\mathrm{Tr}(Y_dY_d^\dagger Y_dY_d^\dagger) - 2\mathrm{Tr}(Y_eY_e^\dagger Y_eY_e^\dagger) - 6\mathrm{Tr}(Y_uY_u^\dagger Y_uY_u^\dagger)\right] + \frac{1}{(16\pi^2)^2}\left[-\frac{3411}{2000}g_1^6 - \frac{1677}{400}g_1^4g_2^2 - \frac{289}{80}g_1^2g_2^4 + \frac{305}{16}g_2^6 + \frac{1887}{200}g_1^4\lambda_1 + \frac{117}{20}g_1^2g_2^2\lambda_1 - \frac{73}{8}g_2^4\lambda_1 + \frac{108}{5}g_1^2\lambda_1^2 + 108g_2^2\lambda_1^2 - 312\lambda_1^3 - 40\lambda_1\lambda_{hs}^2 - 32\lambda_{hs}^3 + \frac{1}{20}(-5(64\lambda_1(-5g_3^2 + 9\lambda_1) - 90g_2^2\lambda_1 + 9g_2^4) + 9g_1^4 + g_1^2(50\lambda_1 + 54g_2^2))\mathrm{Tr}(Y_dY_d^\dagger) - \frac{3}{20}(15g_1^4 - 2g_1^2(11g_2^2 + 25\lambda_1) + 5(-10g_2^2\lambda_1 + 64\lambda_1^2 + g_2^4))\mathrm{Tr}(Y_eY_e^\dagger) - \frac{171}{100}g_1^4\mathrm{Tr}(Y_uY_u^\dagger) + \frac{63}{10}g_1^2g_2^2\mathrm{Tr}(Y_uY_u^\dagger) - \frac{9}{4}g_2^4\mathrm{Tr}(Y_uY_u^\dagger) + \frac{17}{2}g_1^2\lambda_1\mathrm{Tr}(Y_uY_u^\dagger) + \frac{45}{2}g_2^2\lambda_1\mathrm{Tr}(Y_uY_u^\dagger) + 80g_3^2\lambda_1\mathrm{Tr}(Y_uY_u^\dagger) - 144\lambda_1^2\mathrm{Tr}(Y_uY_u^\dagger) + \frac{4}{5}g_1^2\mathrm{Tr}(Y_dY_d^\dagger Y_dY_d^\dagger) - 32g_3^2\mathrm{Tr}(Y_dY_d^\dagger Y_dY_d^\dagger) - 3\lambda_1\mathrm{Tr}(Y_dY_d^\dagger Y_dY_d^\dagger) - 42\lambda\mathrm{Tr}(Y_dY_u^\dagger Y_uY_d^\dagger) - \frac{12}{5}g_1^2\mathrm{Tr}(Y_eY_e^\dagger Y_eY_e^\dagger) - \lambda_1\mathrm{Tr}(Y_eY_e^\dagger Y_eY_e^\dagger) - \frac{8}{5}g_1^2\mathrm{Tr}(Y_uY_u^\dagger Y_uY_u^\dagger) - 32g_3^2\mathrm{Tr}(Y_uY_u^\dagger Y_uY_u^\dagger) - 3\lambda_1\mathrm{Tr}(Y_uY_u^\dagger Y_uY_u^\dagger) + 30\mathrm{Tr}(Y_dY_d^\dagger Y_dY_d^\dagger Y_dY_d^\dagger) - 12\mathrm{Tr}(Y_dY_d^\dagger Y_dY_u^\dagger Y_uY_d^\dagger) + 6\mathrm{Tr}(Y_dY_u^\dagger Y_uY_d^\dagger Y_dY_d^\dagger) - 6\mathrm{Tr}(Y_dY_u^\dagger Y_uY_u^\dagger Y_uY_d^\dagger) + 10\mathrm{Tr}(Y_eY_e^\dagger Y_eY_e^\dagger Y_eY_e^\dagger) + 30\mathrm{Tr}(Y_uY_u^\dagger Y_uY_u^\dagger Y_uY_u^\dagger)\right],$$

$$\beta_{\lambda_s} = \frac{1}{16\pi^2}[20\lambda_t^2 + 8\lambda_{hs}^2] + \frac{1}{(16\pi^2)^2}\left[\frac{16}{5}(3g_1^2\lambda_{hs}^2 + 15g_2^2\lambda_{hs}^2 - 20\lambda_{hs}^3 - 25\lambda_{hs}^2\lambda_t - 75\lambda_t^3 - 15\lambda_{hs}^2\mathrm{Tr}(Y_dY_d^\dagger) - 5\lambda_{hs}^2\mathrm{Tr}(Y_eY_e^\dagger) - 15\lambda_{hs}^2\mathrm{Tr}(Y_uY_u^\dagger))\right],$$

$$\begin{aligned}\beta_{\lambda_{hs}} = {} & \frac{1}{16\pi^2}\left[\frac{1}{10}\lambda_{hs}(120\lambda_1 + 20\mathrm{Tr}(Y_eY_e^\dagger) - 45g_2^2 + 60\mathrm{Tr}(Y_dY_d^\dagger) + 60\mathrm{Tr}(Y_uY_u^\dagger) + 80\lambda_{hs} + 80\lambda_t - 9g_1^2)\right] \\ & + \frac{1}{(16\pi^2)^2}\left[+\frac{1671}{400}g_1^4\lambda_{hs} + \frac{9}{8}g_1^2g_2^2\lambda_{hs} - \frac{145}{16}g_2^4\lambda_{hs} + \frac{72}{5}g_1^2\lambda_1\lambda_{hs} + 72g_2^2\lambda_1\lambda_{hs} - 60\lambda_1^2\lambda_{hs}\right. \\ & + \frac{6}{5}g_1^2\lambda_{hs}^2 + 6g_2^2\lambda_{hs}^2 - 144\lambda_1\lambda_{hs}^2 - 44\lambda_{hs}^3 - 96\lambda_{hs}^2\lambda_t - 40\lambda_{hs}\lambda_t^2 + \frac{1}{4}(32(-3\lambda_{hs} + 5g_3^2 - 9\lambda_1) \\ & + 45g_2^2 + 5g_1^2)\lambda_{hs}\mathrm{Tr}(Y_dY_d^\dagger) + \frac{1}{4}\lambda_{hs}(15g_1^2 + 15g_2^2 - 32(3\lambda_1 + \lambda_{hs}))\mathrm{Tr}(Y_eY_e^\dagger) + \frac{17}{4}g_1^2\lambda_{hs}\mathrm{Tr}(Y_uY_u^\dagger) \\ & + \frac{45}{4}g_2^2\lambda_{hs}\mathrm{Tr}(Y_uY_u^\dagger) + 40g_3^2\lambda_{hs}\mathrm{Tr}(Y_uY_u^\dagger) - 72\lambda_1\lambda_{hs}\mathrm{Tr}(Y_uY_u^\dagger) - 24\lambda_{hs}^2\mathrm{Tr}(Y_uY_u^\dagger) \\ & \left. - \frac{27}{2}\lambda_{hs}\mathrm{Tr}(Y_dY_d^\dagger Y_dY_d^\dagger) - 21\lambda_{hs}\mathrm{Tr}(Y_dY_u^\dagger Y_uY_d^\dagger) - \frac{9}{2}\lambda_{hs}\mathrm{Tr}(Y_eY_e^\dagger Y_eY_e^\dagger) - \frac{27}{2}\lambda_{hs}\mathrm{Tr}(Y_uY_u^\dagger Y_uY_u^\dagger)\right].\end{aligned}$$

[1] G. Aad *et al.* (ATLAS Collaboration), Observation of a new particle in the search for the Standard Model Higgs boson with the ATLAS detector at the LHC, Phys. Lett. B **716**, 1 (2012).

[2] S. Chatrchyan *et al.* (CMS Collaboration), Observation of a new boson at a mass of 125 GeV with the CMS experiment at the LHC, Phys. Lett. B **716**, 30 (2012).

[3] K. Kajantie, M. Laine, K. Rummukainen, and M. Shaposhnikov, The electroweak phase transition: A non-perturbative analysis, Nucl. Phys. **B466**, 189 (1996).

[4] K. Kajantie, M. Laine, K. Rummukainen, and M. Shaposhnikov, Is There a Hot Electroweak Phase Transition at $m_h \gtrsim m_w$, Phys. Rev. Lett. **77**, 2887 (1996).

[5] M. Gurtler, E.-M. Ilgenfritz, and A. Schiller, Where the electroweak phase transition ends, Phys. Rev. D **56**, 3888 (1997).

[6] F. Csikor, Z. Fodor, and J. Heitger, End Point of the Hot Electroweak Phase Transition, Phys. Rev. Lett. **82**, 21 (1999).

[7] M. D'Onofrio, K. Rummukainen, and A. Tranberg, Sphaleron Rate in the Minimal Standard Model, Phys. Rev. Lett. **113**, 141602 (2014).

[8] V. A. Kuzmin, V. A. Rubakov, and M. E. Shaposhnikov, On the anomalous electroweak baryon number nonconservation in the early universe, Phys. Lett. **155B**, 36 (1985).

[9] A. Riotto and M. Trodden, Recent progress in baryogenesis, Annu. Rev. Nucl. Part. Sci. **49**, 35 (1999).

[10] D. E. Morrissey and M. J. Ramsey-Musolf, Electroweak baryogenesis, New J. Phys. **14**, 125003 (2012).

[11] S. Jangid, P. Bandyopadhyay, P. S. Bhupal Dev, and A. Kumar, Vacuum stability in inert higgs doublet model with right-handed neutrinos, J. High Energy Phys. 08 (2020) 154.

[12] S. Jangid and P. Bandyopadhyay, Distinguishing inert Higgs doublet and inert triplet scenarios, Eur. Phys. J. C **80**, 715 (2020).

[13] P. Bandyopadhyay, S. Jangid, and M. Mitra, Scrutinizing vacuum stability in IDM with Type-III inverse seesaw, J. High Energy Phys. 02 (2021) 075.

[14] P. Bandyopadhyay, S. Jangid, and A. Karan, Constraining scalar doublet and triplet leptoquarks with vacuum stability and perturbativity, Eur. Phys. J. C **82**, 516 (2022).

[15] M. Carena, M. Quiros, and C. Wagner, Opening the window for electroweak baryogenesis, Phys. Lett. B **380**, 81 (1996).

[16] M. Quiros, Finite temperature field theory and phase transitions, in *ICTP Summer School in High-Energy Physics and Cosmology* (1999), pp. 187–259, arXiv: hep-ph/9901312.

[17] D. Delepine, J.-M. Gerard, R. Gonzalez Felipe, and J. Weyers, A light stop and electroweak baryogenesis, Phys. Lett. B **386**, 183 (1996).

[18] M. Laine and K. Rummukainen, The MSSM electroweak phase transition on the lattice, Nucl. Phys. **B535**, 423 (1998).

[19] C. Grojean, G. Servant, and J. D. Wells, First-order electroweak phase transition in the Standard Model with a low cutoff, Phys. Rev. D **71**, 036001 (2005).

[20] S. Huber and M. Schmidt, Electroweak baryogenesis: Concrete in a susy model with a gauge singlet, Nucl. Phys. **B606**, 183 (2001).

[21] S. J. Huber, T. Konstandin, T. Prokopec, and M. G. Schmidt, Electroweak phase transition and baryogenesis in the NMSSM, Nucl. Phys. **B757**, 172 (2006).
[22] S. Kanemura, E. Senaha, T. Shindou, and T. Yamada, Electroweak phase transition and Higgs boson couplings in the model based on supersymmetric strong dynamics, J. High Energy Phys. 05 (2013) 066.
[23] K. Cheung, T.-J. Hou, J. S. Lee, and E. Senaha, Singlino-driven electroweak baryogenesis in the next-to-MSSM, Phys. Lett. B **710**, 188 (2012).
[24] S. Kanemura, E. Senaha, and T. Shindou, First-order electroweak phase transition powered by additional F-term loop effects in an extended supersymmetric Higgs sector, Phys. Lett. B **706**, 40 (2011).
[25] C.-W. Chiang and E. Senaha, Electroweak phase transitions in the secluded U(1)-prime-extended MSSM, J. High Energy Phys. 06 (2010) 030.
[26] M. Carena, G. Nardini, M. Quiros, and C. E. M. Wagner, MSSM electroweak baryogenesis and LHC data, J. High Energy Phys. 02 (2013) 001.
[27] G. F. Giudice, Electroweak phase transition in supersymmetry, Phys. Rev. D **45**, 3177 (1992).
[28] S. Myint, Baryogenesis constraints on the minimal supersymmetric model, Phys. Lett. B **287**, 325 (1992).
[29] T. A. Chowdhury, M. Nemevsek, G. Senjanovic, and Y. Zhang, Dark matter as the trigger of strong electroweak phase transition, J. Cosmol. Astropart. Phys. 02 (2012) 029.
[30] D. Borah and J. M. Cline, Inert doublet dark matter with strong electroweak phase transition, Phys. Rev. D **86**, 055001 (2012).
[31] G. Gil, P. Chankowski, and M. Krawczyk, Inert dark matter and strong electroweak phase transition, Phys. Lett. B **717**, 396 (2012).
[32] S. S. AbdusSalam and T. A. Chowdhury, Scalar representations in the light of electroweak phase transition and cold dark matter phenomenology, J. Cosmol. Astropart. Phys. 05 (2014) 026.
[33] J. M. Cline and K. Kainulainen, Improved electroweak phase transition with subdominant inert doublet dark matter, Phys. Rev. D **87**, 071701 (2013).
[34] V. Vaskonen, Electroweak baryogenesis and gravitational waves from a real scalar singlet, Phys. Rev. D **95**, 123515 (2017).
[35] S. Profumo, M. J. Ramsey-Musolf, and G. Shaughnessy, Singlet Higgs phenomenology and the electroweak phase transition, J. High Energy Phys. 08 (2007) 010.
[36] A. Ahriche, What is the criterion for a strong first order electroweak phase transition in singlet models?, Phys. Rev. D **75**, 083522 (2007).
[37] J. R. Espinosa, T. Konstandin, and F. Riva, Strong electroweak phase transitions in the standard model with a singlet, Nucl. Phys. **B854**, 592 (2012).
[38] J. M. Cline and K. Kainulainen, Electroweak baryogenesis and dark matter from a singlet Higgs, J. Cosmol. Astropart. Phys. 01 (2013) 012.
[39] J. M. Cline, K. Kainulainen, P. Scott, and C. Weniger, Update on scalar singlet dark matter, Phys. Rev. D **88**, 055025 (2013); **92**, 039906(E) (2015).
[40] V. Barger, P. Langacker, M. McCaskey, M. Ramsey-Musolf, and G. Shaughnessy, Complex singlet extension of the Standard Model, Phys. Rev. D **79**, 015018 (2009).
[41] M. Gonderinger, H. Lim, and M. J. Ramsey-Musolf, Complex scalar singlet dark matter: Vacuum stability and phenomenology, Phys. Rev. D **86**, 043511 (2012).
[42] A. Ahriche and S. Nasri, Light dark matter, light Higgs and the electroweak phase transition, Phys. Rev. D **85**, 093007 (2012).
[43] T. Brauner, T. V. I. Tenkanen, A. Tranberg, A. Vuorinen, and D. J. Weir, Dimensional reduction of the standard model coupled to a new singlet scalar field, J. High Energy Phys. 03 (2017) 007.
[44] M. Carena, Z. Liu, and Y. Wang, Electroweak phase transition with spontaneous Z_2-breaking, J. High Energy Phys. 08 (2020) 107.
[45] M. Carena, Z. Liu, and M. Riembau, Probing the electroweak phase transition via enhanced di-Higgs boson production, Phys. Rev. D **97**, 095032 (2018).
[46] P. Ghorbani, Vacuum structure and electroweak phase transition in singlet scalar dark matter, Phys. Dark Universe **33**, 100861 (2021).
[47] K. Ghorbani and P. H. Ghorbani, Strongly first-order phase transition in real singlet scalar dark matter model, arXiv:1804.05798.
[48] P. M. Schicho, T. V. I. Tenkanen, and J. Österman, Robust approach to thermal resummation: Standard model meets a singlet, J. High Energy Phys. 06 (2021) 130.
[49] L. Niemi, P. Schicho, and T. V. Tenkanen, Singlet-assisted electroweak phase transition at two loops, Phys. Rev. D **103**, 115035 (2021).
[50] K. Fuyuto and E. Senaha, Improved sphaleron decoupling condition and the Higgs coupling constants in the real singlet-extended Standard Model, Phys. Rev. D **90**, 015015 (2014).
[51] G. C. Dorsch, S. J. Huber, and J. M. No, A strong electroweak phase transition in the 2HDM after LHC8, J. High Energy Phys. 10 (2013) 029.
[52] S. Kanemura, Y. Okada, and E. Senaha, Electroweak baryogenesis and the triple Higgs boson coupling, eConf **C050318**, 0704 (2005).
[53] J. O. Andersen, T. Gorda, A. Helset, L. Niemi, T. V. I. Tenkanen, A. Tranberg, and D. J. Weir, Nonperturbative Analysis of the Electroweak Phase Transition in the Two Higgs Doublet Model, Phys. Rev. Lett. **121**, 191802 (2018).
[54] B. Barman, A. Dutta Banik, and A. Paul, Singlet-doublet fermionic dark matter and gravitational waves in a two-Higgs-doublet extension of the Standard Model, Phys. Rev. D **101**, 055028 (2020).
[55] H. H. Patel and M. J. Ramsey-Musolf, Stepping into electroweak symmetry breaking: Phase transitions and Higgs phenomenology, Phys. Rev. D **88**, 035013 (2013).
[56] M. J. Kazemi and S. S. Abdussalam, Electroweak phase transition in an inert complex triplet model, Phys. Rev. D **103**, 075012 (2021).
[57] L. Niemi, H. H. Patel, M. J. Ramsey-Musolf, T. V. I. Tenkanen, and D. J. Weir, Electroweak phase transition in the real triplet extension of the SM: Dimensional reduction, Phys. Rev. D **100**, 035002 (2019).

[58] G.-C. Cho, C. Idegawa, and E. Senaha, Electroweak phase transition in a complex singlet extension of the Standard Model with degenerate scalars, Phys. Lett. B **823**, 136787 (2021).
[59] C.-W. Chiang, Y.-T. Li, and E. Senaha, Revisiting electroweak phase transition in the Standard Model with a real singlet scalar, Phys. Lett. B **789**, 154 (2019).
[60] A. Paul, B. Banerjee, and D. Majumdar, Gravitational wave signatures from an extended inert doublet dark matter model, J. Cosmol. Astropart. Phys. 10 (2019) 062.
[61] N. F. Bell, M. J. Dolan, L. S. Friedrich, M. J. Ramsey-Musolf, and R. R. Volkas, A real triplet-singlet extended standard model: Dark matter and collider phenomenology, J. High Energy Phys. 04 (2021) 098.
[62] V. R. Shajiee and A. Tofighi, Electroweak phase transition, gravitational waves and dark matter in two scalar singlet extension of the standard model, Eur. Phys. J. C **79**, 360 (2019).
[63] E. Hall, T. Konstandin, R. McGehee, H. Murayama, and G. Servant, Baryogenesis from a dark first-order phase transition, J. High Energy Phys. 04 (2020) 042.
[64] M. Garcia-Pepin and M. Quiros, Strong electroweak phase transition from Supersymmetric Custodial Triplets, J. High Energy Phys. 05 (2016) 177.
[65] A. Linde, Decay of the false vacuum at finite temperature, Nucl. Phys. **B216**, 421 (1983).
[66] E. Witten, Cosmic separation of phases, Phys. Rev. D **30**, 272 (1984).
[67] C. J. Hogan, Gravitational radiation from cosmological phase transitions, Mon. Not. R. Astron. Soc. **218**, 629 (1986).
[68] C. Caprini *et al.*, Detecting gravitational waves from cosmological phase transitions with LISA: An update, J. Cosmol. Astropart. Phys. 03 (2020) 024.
[69] O. Gould, J. Kozaczuk, L. Niemi, M. J. Ramsey-Musolf, T. V. I. Tenkanen, and D. J. Weir, Nonperturbative analysis of the gravitational waves from a first-order electroweak phase transition, Phys. Rev. D **100**, 115024 (2019).
[70] D. J. Weir, Gravitational waves from a first order electroweak phase transition: A brief review, Phil. Trans. R. Soc. A **376**, 20170126 (2018).
[71] M. Hindmarsh, S. J. Huber, K. Rummukainen, and D. J. Weir, Shape of the acoustic gravitational wave power spectrum from a first order phase transition, Phys. Rev. D **96**, 103520 (2017); **101**, 089902(E) (2020).
[72] H.-K. Guo, K. Sinha, D. Vagie, and G. White, Phase transitions in an expanding universe: Stochastic gravitational waves in standard and non-standard histories, J. Cosmol. Astropart. Phys. 01 (2021) 001.
[73] M. Hindmarsh, S. Huber, K. Rummukainen, and D. Weir, Gravitational waves from cosmological first order phase transitions, Proc. Sci., LATTICE2015 (**2016**) 233.
[74] P. Bandyopadhyay and A. Costantini, Obscure Higgs boson at colliders, Phys. Rev. D **103**, 015025 (2021).
[75] P. Bandyopadhyay, S. Jangid, A. KT, and S. Parashar, Discerning the Triplet charged Higgs bosons in BSM scenarios at the LHC and MATHUSLA (to be published).
[76] P. Bandyopadhyay, K. Huitu, and A. Sabanci, Status of $Y = 0$ triplet Higgs with supersymmetry in the light of ~125 GeV Higgs discovery, J. High Energy Phys. 10 (2013) 091.
[77] P. Bandyopadhyay, C. Coriano, and A. Costantini, Probing the hidden Higgs bosons of the $Y = 0$ triplet- and singlet-extended Supersymmetric Standard Model at the LHC, J. High Energy Phys. 12 (2015) 127.
[78] P. Bandyopadhyay, C. Coriano, and A. Costantini, Perspectives on a supersymmetric extension of the standard model with a $Y = 0$ Higgs triplet and a singlet at the LHC, J. High Energy Phys. 09 (2015) 045.
[79] P. Bandyopadhyay, S. Di Chiara, K. Huitu, and A. S. Keçeli, Naturality vs perturbativity, B_s physics, and LHC data in triplet extension of MSSM, J. High Energy Phys. 11 (2014) 062.
[80] P. Bandyopadhyay, K. Huitu, and A. Sabanci Keceli, Multi-lepton signatures of the triplet like charged Higgs at the LHC, J. High Energy Phys. 05 (2015) 026.
[81] P. Bandyopadhyay and A. Costantini, Distinguishing charged Higgs bosons from different representations at the LHC, J. High Energy Phys. 01 (2018) 067.
[82] P. Bandyopadhyay, C. Coriano, and A. Costantini, General analysis of the charged Higgs sector of the $Y = 0$ triplet-singlet extension of the MSSM at the LHC, Phys. Rev. D **94**, 055030 (2016).
[83] A. Sabanci Keceli, P. Bandyopadhyay, and K. Huitu, Long-lived triplinos and displaced lepton signals at the LHC, Eur. Phys. J. C **79**, 345 (2019).
[84] J. R. Espinosa and M. Quiros, The electroweak phase transition with a singlet, Phys. Lett. B **305**, 98 (1993).
[85] K. Yagi and N. Seto, Detector configuration of DECIGO/BBO and identification of cosmological neutron-star binaries, Phys. Rev. D **83**, 044011 (2011); **95**, 109901(E) (2017).
[86] P. Amaro-Seoane *et al.* (LISA Collaboration), Laser interferometer space antenna, arXiv:1702.00786.
[87] B. P. Abbott *et al.*, Prospects for observing and localizing gravitational-wave transients with Advanced LIGO, Advanced Virgo and KAGRA, Living Rev. Relativity **21**, 3 (2018).
[88] B. P. Abbott *et al.* (LIGO Scientific Collaboration and Virgo Collaboration), Observation of Gravitational Waves from a 22-Solar-Mass Binary Black Hole Coalescence, Phys. Rev. Lett. **116**, 241103 (2016).
[89] B. P. Abbott *et al.* (LIGO Scientific and Virgo Collaborations), Observation of a 50-Solar-Mass Binary Black Hole Coalescence at Redshift 0.2, Phys. Rev. Lett. **118**, 221101 (2017).
[90] S. Coleman and E. Weinberg, Radiative corrections as the origin of spontaneous symmetry breaking, Phys. Rev. D **7**, 1888 (1973).
[91] S. Weinberg, Gauge and global symmetries at high temperature, Phys. Rev. D **9**, 3357 (1974).
[92] L. Dolan and R. Jackiw, Symmetry behavior at finite temperature, Phys. Rev. D **9**, 3320 (1974).
[93] D. A. Kirzhnits and A. D. Linde, Symmetry behavior in gauge theories, Ann. Phys. (N.Y.) **101**, 195 (1976).
[94] D. J. Gross, R. D. Pisarski, and L. G. Yaffe, QCD and instantons at finite temperature, Rev. Mod. Phys. **53**, 43 (1981).

[95] P. Fendley, The effective potential and the coupling constant at high temperature, Phys. Lett. B **196**, 175 (1987).
[96] J. Kapusta, *Finite Temperature Field Theory* (Cambridge University Press, Cambridge, England, 1989).
[97] P. B. Arnold and O. Espinosa, The effective potential and first order phase transitions: Beyond leading-order, Phys. Rev. D **47**, 3546 (1993).
[98] L. Niemi, P. Schicho, and T. V. I. Tenkanen, Singlet-assisted electroweak phase transition at two loops, Phys. Rev. D **103**, 115035 (2021).
[99] P. A. Zyla *et al.* (Particle Data Group), Review of particle physics, Prog. Theor. Exp. Phys. **2020**, 083C01 (2020).
[100] A. Cohen, D. Kaplan, and A. Nelson, Progress in electroweak baryogenesis, Annu. Rev. Nucl. Part. Sci. **43**, 27 (1994).
[101] V. A. Rubakov and M. E. Shaposhnikov, Electroweak baryon number nonconservation in the early universe and in high-energy collisions, Usp. Fiz. Nauk **166**, 493 (1996).
[102] F. Staub, SARAH 4: A tool for (not only SUSY) model builders, Comput. Phys. Commun. **185**, 1773 (2014).
[103] M. Carena, G. Nardini, M. Quiros, and C. E. M. Wagner, The baryogenesis window in the MSSM, Nucl. Phys. **B812**, 243 (2009).
[104] J. R. Espinosa, Dominant two loop corrections to the MSSM finite temperature effective potential, Nucl. Phys. **B475**, 273 (1996).
[105] M. Carena, M. Quiros, and C. E. M. Wagner, Electroweak baryogenesis and Higgs and stop searches at LEP and the tevatron, Nucl. Phys. **B524**, 3 (1998).
[106] M. Laine, M. Meyer, and G. Nardini, Thermal phase transition with full 2-loop effective potential, Nucl. Phys. **B920**, 565 (2017).
[107] O. Gould and T. V. I. Tenkanen, On the perturbative expansion at high temperature and implications for cosmological phase transitions, J. High Energy Phys. 06 (2021) 069.
[108] K. Farakos, K. Kajantie, K. Rummukainen, and M. E. Shaposhnikov, 3-D physics and the electroweak phase transition: Perturbation theory, Nucl. Phys. **B425**, 67 (1994).
[109] P. M. Schicho, T. V. I. Tenkanen, and J. Österman, Robust approach to thermal resummation: Standard Model meets a singlet, J. High Energy Phys. 06 (2021) 130.
[110] L. Niemi, H. H. Patel, M. J. Ramsey-Musolf, T. V. I. Tenkanen, and D. J. Weir, Electroweak phase transition in the real triplet extension of the SM: Dimensional reduction, Phys. Rev. D **100**, 035002 (2019).
[111] P. A. R. Ade *et al.* (Planck Collaboration), Planck 2013 results. XVI. Cosmological parameters, Astron. Astrophys. **571**, A16 (2014).
[112] P. Bandyopadhyay and A. Costantini, Exploring the Complex Scalar Extensions of the Standard Model (to be published).
[113] T. Robens and T. Stefaniak, Status of the Higgs singlet extension of the standard model after LHC run 1, Eur. Phys. J. C **75**, 104 (2015).
[114] C. Wainwright and S. Profumo, The impact of a strongly first-order phase transition on the abundance of thermal relics, Phys. Rev. D **80**, 103517 (2009).
[115] C. L. Wainwright, Cosmo transitions, Comput. Phys. Commun. **183** (2006).
[116] P. Athron, C. Balazs, M. Bardsley, A. Fowlie, D. Harries, and G. White, BubbleProfiler: Finding the field profile and action for cosmological phase transitions, Comput. Phys. Commun. **244**, 448 (2019).
[117] L. Randall and G. Servant, Gravitational waves from warped spacetime, J. High Energy Phys. 05 (2007) 054.
[118] A. Kosowsky, M. S. Turner, and R. Watkins, Gravitational radiation from colliding vacuum bubbles, Phys. Rev. D **45**, 4514 (1992).
[119] A. Kosowsky and M. S. Turner, Gravitational radiation from colliding vacuum bubbles: Envelope approximation to many-bubble collisions, Phys. Rev. D **47**, 4372 (1993).
[120] S. J. Huber and T. Konstandin, Gravitational wave production by collisions: more bubbles, J. Cosmol. Astropart. Phys. 09 (2008) 022.
[121] A. Kosowsky, M. S. Turner, and R. Watkins, Gravitational Waves from First-Order Cosmological Phase Transitions, Phys. Rev. Lett. **69**, 2026 (1992).
[122] M. Kamionkowski, A. Kosowsky, and M. S. Turner, Gravitational radiation from first-order phase transitions, Phys. Rev. D **49**, 2837 (1994).
[123] C. Caprini, R. Durrer, and G. Servant, Gravitational wave generation from bubble collisions in first-order phase transitions: An analytic approach, Phys. Rev. D **77**, 124015 (2008).
[124] M. Hindmarsh, S. J. Huber, K. Rummukainen, and D. J. Weir, Gravitational Waves from the Sound of a First Order Phase Transition, Phys. Rev. Lett. **112**, 041301 (2014).
[125] L. Leitao, A. Megevand, and A. D. Sanchez, Gravitational waves from the electroweak phase transition, J. Cosmol. Astropart. Phys. 10 (2012) 024.
[126] J. T. Giblin, Jr. and J. B. Mertens, Vacuum bubbles in the presence of a relativistic fluid, J. High Energy Phys. 12 (2013) 042.
[127] J. T. Giblin and J. B. Mertens, Gravitional radiation from first-order phase transitions in the presence of a fluid, Phys. Rev. D **90**, 023532 (2014).
[128] M. Hindmarsh, S. J. Huber, K. Rummukainen, and D. J. Weir, Numerical simulations of acoustically generated gravitational waves at a first order phase transition, Phys. Rev. D **92**, 123009 (2015).
[129] C. Caprini and R. Durrer, Gravitational waves from stochastic relativistic sources: Primordial turbulence and magnetic fields, Phys. Rev. D **74**, 063521 (2006).
[130] T. Kahniashvili, A. Kosowsky, G. Gogoberidze, and Y. Maravin, Detectability of gravitational waves from phase transitions, Phys. Rev. D **78**, 043003 (2008).
[131] T. Kahniashvili, L. Campanelli, G. Gogoberidze, Y. Maravin, and B. Ratra, Gravitational radiation from primordial helical inverse cascade MHD turbulence, Phys. Rev. D **78**, 123006 (2008); **79**, 109901(E) (2009).
[132] T. Kahniashvili, L. Kisslinger, and T. Stevens, Gravitational radiation generated by magnetic fields in cosmological phase transitions, Phys. Rev. D **81**, 023004 (2010).
[133] C. Caprini, R. Durrer, and G. Servant, The stochastic gravitational wave background from turbulence and magnetic fields generated by a first-order phase transition, J. Cosmol. Astropart. Phys. 12 (2009) 024.
[134] C. Caprini *et al.*, Science with the space-based interferometer eLISA. II: Gravitational waves from cosmological

phase transitions, J. Cosmol. Astropart. Phys. 04 (2016) 001.
[135] W. Chao, H.-K. Guo, and J. Shu, Gravitational wave signals of electroweak phase transition triggered by dark matter, J. Cosmol. Astropart. Phys. 09 (2017) 009.
[136] P. S. B. Dev, F. Ferrer, Y. Zhang, and Y. Zhang, Gravitational waves from first-order phase transition in a simple axion-like particle model, J. Cosmol. Astropart. Phys. 11 (2019) 006.
[137] P. J. Steinhardt, Relativistic detonation waves and bubble growth in false vacuum decay, Phys. Rev. D **25**, 2074 (1982).
[138] V. R. Shajiee and A. Tofighi, Electroweak phase transition, gravitational waves and dark matter in two scalar singlet extension of the standard model, Eur. Phys. J. C **79**, 360 (2019).
[139] M. Kamionkowski, A. Kosowsky, and M. S. Turner, Gravitational radiation from first order phase transitions, Phys. Rev. D **49**, 2837 (1994).
[140] J. Ellis, M. Lewicki, and J. M. No, On the maximal strength of a first-order electroweak phase transition and its gravitational wave signal, J. Cosmol. Astropart. Phys. 04 (2019) 003.
[141] J. R. Espinosa, T. Konstandin, J. M. No, and G. Servant, Energy budget of cosmological first-order phase transitions, J. Cosmol. Astropart. Phys. 06 (2010) 028.
[142] B. C. Barish, S. Bird, and Y. Cui, Impact of a midband gravitational wave experiment on detectability of cosmological stochastic gravitational wave backgrounds, Phys. Rev. D **103**, 123541 (2021).
[143] M. Aoki and J. Kubo, Gravitational waves from chiral phase transition in a conformally extended standard model, J. Cosmol. Astropart. Phys. 04 (2020) 001.
[144] K. Yagi, Scientific potential of DECIGO pathfinder and testing GR with space-borne gravitational wave interferometers, Int. J. Mod. Phys. D **22**, 1341013 (2013).
[145] C. J. Moore, R. H. Cole, and C. P. L. Berry, Gravitational-wave sensitivity curves, Classical Quantum Gravity **32**, 015014 (2015).
[146] K. Yagi, N. Tanahashi, and T. Tanaka, Probing the size of extra dimension with gravitational wave astronomy, Phys. Rev. D **83**, 084036 (2011).
[147] E. Thrane and J. D. Romano, Sensitivity curves for searches for gravitational-wave backgrounds, Phys. Rev. D **88**, 124032 (2013).
[148] D. Croon, O. Gould, P. Schicho, T. V. I. Tenkanen, and G. White, Theoretical uncertainties for cosmological first-order phase transitions, J. High Energy Phys. 04 (2021) 055.
[149] P. M. Stevenson, Optimized perturbation theory, Phys. Rev. D **23**, 2916 (1981).